

A pore-scale numerical framework for solute transport and dispersion in porous media

Yang Liu, Wenbo Gong, Han Xiao, Moran Wang^{*}

Department of Engineering Mechanics, Tsinghua University, Beijing 100084, China

ARTICLE INFO

Keywords:

Solute transport
Porous media
Pore network model
Pore-scale shear dispersion

ABSTRACT

Pore-scale modeling plays a crucial role in understanding and upscaling solute transport behavior in porous media. Direct simulation offers the highest fidelity in resolving pore-scale fluid flow and mass transfer, nevertheless, with unacceptable computational costs for practical applications. Pore network models (PNM), on the other hand, provide an efficient alternative but with reduced accuracy in representing transport dynamics. In this study, we propose a new framework of pore network models that ensures both accuracy and efficiency, which reproduces the pore-scale shear dispersion effect by utilizing the pore-scale shear dispersion coefficient to calculate the diffusive mass exchange rate between network elements. The coefficient is determined based on the extension of Taylor-Aris theory that expands the classical Taylor-Aris theory to encompass the pre-asymptotic regime. Additionally, the framework adopts a physically representative pore network, where the conduit length and volume of network elements are determined based on local resistance equivalence. After verifying its accuracy and reliability, we conduct a series of numerical cases on tube networks, sphere packs, and sand packs. The breakthrough curves and concentration profiles obtained from our new model show good agreement with direct simulation results and experimental data, while the simulation outcomes of the models that rely on the molecular diffusion coefficient or Taylor dispersion coefficient for local mass exchange may exhibit significant errors. We finally demonstrate that the significance of pore-scale shear dispersion on solute transport weakens for tube networks with increasing degrees of geometrical disorder. The proposed model provides an accurate and efficient numerical framework for the study of solute transport and dispersion in porous media.

1. Introduction

Understanding of solute transport in porous media is important to numerous natural processes and industrial applications, including contaminant hydrogeology (Bear, 2013), brain microcirculation (Berg et al., 2020), geological carbon dioxide storage (Mehmani and Xu, 2022), and the design of batteries (van Gorp et al., 2023). The homogenized manifestation of solute transport, dispersion, originates from the averaging of velocity variations that cannot be resolved at the homogenization scale. Any velocity variations below this scale contribute to enhanced dispersion (Dentz and de Barros, 2015). Phenomena giving rise to dispersion in porous media include molecular diffusion, advection, and mechanical dispersion (Bear, 2013). Molecular diffusion is the random thermal motion of solute molecules or particles. Mechanical dispersion arises from variability in the flow field and the repeated separation and merging of flow passages. Advection, on the other hand, refers to the bulk movement of solutes or particles with the fluid.

Advection propelled by non-uniform velocities within the pores, such as velocity gradients caused by no-slip condition at the walls, enhances dispersion, an effect known as shear dispersion (Saffman, 1959; Koch and Brady, 1985; Hidalgo and Dentz, 2018). Pore-scale shear dispersion is inevitable due to the complicated conditions at fluid-solid interfaces. The study of shear dispersion in a capillary tube has been addressed through analytical solutions by Aris (1956), and Taylor (1953). However, these analyses were limited to the asymptotic regime, which assumes sufficiently long tubes. In reality, the asymptotic regime is often unattainable, especially for porous media flow, where shear dispersion is typically pre-asymptotic (Ananthkrishnan et al., 1965; Taghizadeh et al., 2020; Puyguraud et al., 2019; Dentz et al., 2018; Mauri and Haber, 1991). Accurately describing pre-asymptotic shear dispersion poses significant challenges and remains an active area of research.

Pore-scale modeling is a powerful tool for understanding solute transport in porous media by capturing pore-scale physics (Dentz et al., 2011). Pore-scale modeling methods for flow and transport in porous

^{*} Corresponding author.

E-mail address: mrwang@tsinghua.edu.cn (M. Wang).

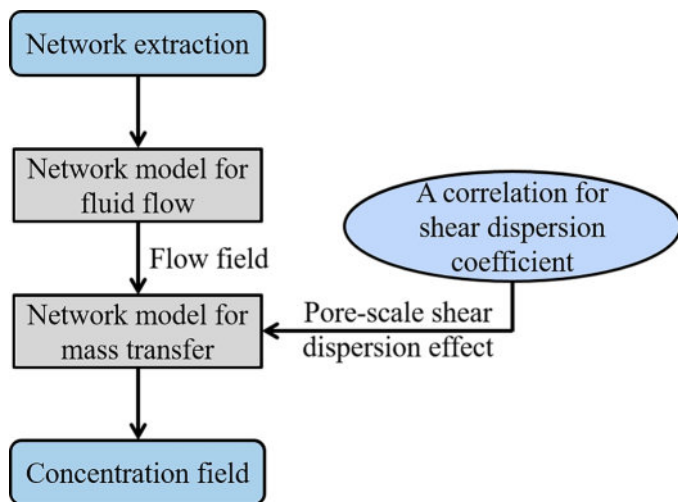


Fig. 1. Flowchart of the proposed pore-network framework for solute transport and dispersion in porous media.

media can be broadly classified into two groups: direct numerical simulation (DNS) and pore network models (PNM) (Blunt et al., 2013; Golparvar et al., 2018; Yang et al., 2016). DNS directly solves the governing equations of flow and transport using methods such as finite volume methods (FVM) (Ferrari and Lunati, 2014; Kou et al., 2023; Cheng et al., 2022; Yang et al., 2013), smoothed particle hydrodynamics (SPH) (Tartakovsky et al., 2007), and lattice Boltzmann methods (LBM) (Xie et al., 2021; Zheng et al., 2018; Chen and Doolen, 1998; Roslin et al., 2019; Yan et al., 2017). Although DNS yields the highest fidelity resolution of fluid flow and mass transfer, it is computationally expensive. On the other hand, PNM simulates flow and transport on representative networks derived from pore structures (Liu et al., 2022; Khayrat and Jenny, 2017; Weishaupt et al., 2019; Chen et al., 2021; Chen et al., 2020; Khayrat et al., 2018; Zhang et al., 2015; Wang et al., 2020; He et al., 2021). By reducing the complexity of pore structures to network elements, PNM calculates the transport properties of network elements analytically or semi-analytically. Consequently, PNM offers a significant advantage over DNS in terms of computational efficiency. Additionally, there are emerging multi-scale simulation methods (Mehmani and Tchelepi, 2018; Guo et al., 2019; Mehmani and Tchelepi, 2019; Mehmani et al., 2021; Li and Mehmani, 2023; Mehmani and Li, 2023; Liu et al., 2022) that aim to strike a balance between computational efficiency and accuracy. In this study, we focus on the pore network model.

Pore network models for solute transport in porous media can be categorized into two types: the particle tracking-based pore network model (PT-PNM) and the mixed-cell method-based pore network model (MCM-PNM). PT-PNM inherently captures the pore-scale shear dispersion effect, but it demands significant computational resources due to the requirement of a large number of particles for statistically converged results (Bijeljic et al., 2004; Raman et al., 2011; Sahimi et al., 1986). In contrast, MCM-PNM is computationally efficient but has limitations in properly accounting for the pore-scale shear dispersion effect, as it does not incorporate the intricate influence of non-uniform velocity profiles in cross-sections. With exceptional computational performance, MCM-PNM has gained wide popularity for studying solute transport in porous media (Mehmani and Xu, 2022; Kim et al., 2011; Koplik et al., 1988; Li et al., 2006; Sadeghi et al., 2017; Sadeghi et al., 2020; Esteves et al., 2020; Acharya et al., 2007; Sahimi and Jue, 1989; Li et al., 2014; Bernabé et al., 2016; Babaei and Joekar-Niasar, 2016; Mehmani and Balhoff, 2015). However, the treatment of the pore-scale shear dispersion effect in these studies varies significantly and can be broadly classified into two categories. The first category of MCM-PNM disregards pore-scale shear dispersion, where the diffusive mass exchange rate

between network elements is calculated solely based on the molecular diffusion coefficient (Kim et al., 2011; Koplik et al., 1988; Li et al., 2006; Sadeghi et al., 2017; Sadeghi et al., 2020; Esteves et al., 2020; Acharya et al., 2007). On the other hand, the second category of MCM-PNM incorporates the classical Taylor-Aris theory (Aris, 1956; Taylor, 1953), where the Taylor dispersion coefficient is utilized to calculate the diffusive mass exchange rate between network elements (Sahimi and Jue, 1989; Li et al., 2014; Bernabé et al., 2016; Babaei and Joekar-Niasar, 2016). Both treatments, namely, neglecting pore-scale shear dispersion or relying on Taylor dispersion, are physically unrealistic and consequently can lead to significant errors in simulation outcomes. In addition to the aforementioned approaches, Mehmani et al. (Mehmani and Balhoff, 2015) introduced the superposing transport method to capture the pore-scale shear dispersion effect, where the total mass exchange rate between a pore and a throat is calculated based on semi-empirical elementary response functions and the evolutionary histories of the concentration. This method provides a more accurate consideration of pore-scale shear dispersion compared to the aforementioned two categories of MCM-PNM, while, at the same time, bringing certain limitations. Firstly, it requires intensive memory and computation resources, which can be a practical constraint for large-scale simulations. Secondly, the elementary response functions within the method are limited to network elements with circular cross-sections, which may be inadequate to represent the complexity of real porous media with irregular geometries. In summary, existing studies suffer from the following drawbacks: while different treatments of pore-scale shear dispersion in MCM-PNM have been reported, they either lack substantial validation of their applicability or exhibit notably low computational efficiency. Therefore, there remains an absence of a pore network model for solute transport through porous media that integrates both accuracy and efficiency.

In this work, a pore network framework for solute transport in porous media is proposed and validated. To reproduce the pore-scale shear dispersion effect, the present model determines the diffusive mass exchange rate between network elements based on the pore-scale shear dispersion coefficient. This coefficient is determined based on the extension of Taylor-Aris theory (Taylor, 1953; Ananthkrishnan et al., 1965) to encompass the pre-asymptotic regime. In the new model, both pores and throats contribute to the resistance and volumes, and their values are determined by LoREPorTS (Liu et al., 2022), a pore-throat segmentation method based on local resistance equivalence. We validate the present model through a series of numerical cases and assess the accuracy of the other methods, neglecting pore-scale shear dispersion or relying on Taylor dispersion. Finally, we discuss the significance of pore-scale shear dispersion on solute transport, utilizing tube networks with varying degrees of geometrical disorder.

The remainder of this paper is structured as follows. In Section 2, a comprehensive description of the proposed pore network model and the extension of Taylor-Aris theory are presented. Section 3 focuses on the validation through cases involving DNS solutions and experimental data. In Section 4, we utilize the present model to discuss the impact of pore-scale shear dispersion on solute transport under different geometrical disorders. Finally, the conclusions are drawn in Section 5.

2. Model elaboration

In this section, we present the details of the proposed pore network framework for solute transport and dispersion in porous media. After the network extraction, the transport simulation procedure, as Fig. 1 shows, consists of two steps: firstly, solving the flow field to determine the flow rates between adjacent pores, and secondly, modeling mass transfer to dynamically update the concentration within each network element. It is worth mentioning that PNM reduces the mass transfer between adjacent pores to one-dimensional ones, thereby neglecting the intricate influence of non-uniform velocity profiles in cross-sections. The present model incorporates the pore-scale shear dispersion coefficients, instead

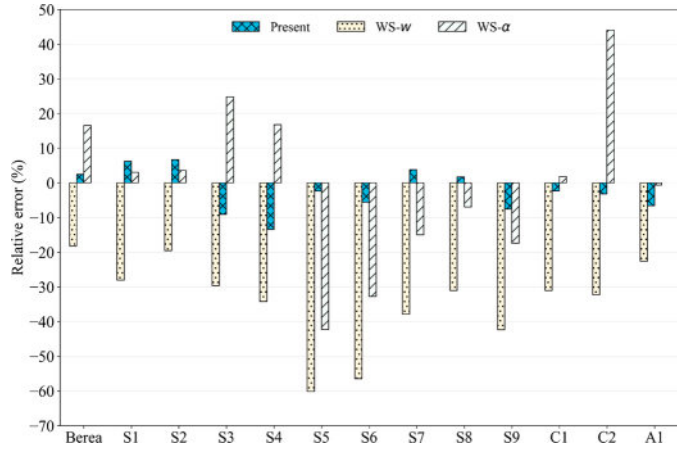


Fig. 2. The relative errors in the predicted absolute permeability by different models. ‘Present’ stands for the results predicted by the present model. ‘WS – w’, and ‘WS – α ’ denote the results predicted by the models where the w method (Liu et al., 2022; Sholokhova et al., 2009) and the α method (Liu et al., 2022; Øren and Bakke, 2003; Dong and Blunt, 2009) are used for pore-throat segmentation. Samples include sandstone (Berea and S1-S9), carbonate (C1-C2), and sand pack (A1) (Dong and Blunt, 2009).

of the intrinsic diffusion coefficients, to calculate the diffusive mass exchange rate between network elements in the simulation of mass transfer, which are determined by a correlation for shear dispersion, extending the Taylor-Aris theory.

2.1. Network model for fluid flow

The conduit lengths and volumes of network elements have a significant impact on the predicted flow and transport properties (Bhattad et al., 2011; Bondino et al., 2013). In this model, both pores and throats contribute to the resistance and volumes. We employ the LoREPorTS (Liu et al., 2022) algorithm, a pore-throat segmentation method based on local resistance equivalence, to extract pore networks from the pore structures.

In the present model, we considered network elements with circular, square, and triangular cross-sectional shapes, characterized by the dimensionless shape factor $G = R^2/4A$, where R is the inscribed diameter and A is the cross-sectional area (Mason and Morrow, 1991; Bultreys et al., 2018). The hydraulic conductance of an individual network element is calculated using the equation:

$$g = \frac{kGA^2}{\mu l}, \quad (1)$$

where l is the hydraulic conduit length and k is a coefficient dependent on the cross-sectional shape. The conduit length l of pores and throats is one of the key parameters in the determination of conductance g , which ultimately affects the accuracy of permeability prediction. When extracting pore networks from pore structures, both the conduit length l and volume are determined by LoREPorTS (Liu et al., 2022), a pore-throat segmentation method based on local resistance equivalence. More specifically, first, the hydraulic radii along the skeleton connecting neighboring pores are determined from the pore space. Next, the flow resistance of each cross-section segment, each with a voxel length, is calculated based on the assumption of Poiseuille flow. The total hydraulic resistance is then obtained by summing up the flow resistance of each individual segment. Subsequently, the interfaces between pores and throats are carefully located at the position where the network elements preserve the local hydraulic resistance of the real space best. The conduit length is defined as the distance between the interfaces at the two ends of a pore or throat. The volume of a pore or throat is determined by counting the number of voxels within it. The cross-sectional

area A is determined by counting the number of voxels at the interface, while the inscribed radius R is determined by maximum Euclidean distance of the voxels at the interface. For more details on the determination of the above parameters in LoREPorTS, please refer to our previous work (Liu et al., 2022). For network elements with triangular ($0 < G \leq \frac{\sqrt{3}}{36}$), square ($\frac{\sqrt{3}}{36} < G < \frac{1}{4\pi}$), and circular ($G \geq \frac{1}{4\pi}$) cross-sectional shapes, the corresponding values of k are 0.6, 0.5623, and 0.5 (Patzek and Silin, 2001), respectively. Two adjacent pores are connected by three network elements, including the pores located at both ends and the throats between them. The conductance between two adjacent pores is determined by taking the harmonic mean of the conductance of each element,

$$g_{ij} = \frac{1}{\frac{1}{g_i} + \frac{1}{g_t} + \frac{1}{g_j}}, \quad (2)$$

where t indicates the throat and i and j represent pores, respectively. The flow rate between pore i and pore j is given by

$$q_{ij} = g_{ij}(P_i - P_j), \quad (3)$$

where P_i and P_j stand for the pressure in pore i and pore j , respectively. Given a pressure drop of ΔP between the inlet and outlet of the network, the pressure in pores can be solved by applying mass conservation at each pore. Consider pore i , for instance:

$$\sum_j q_{ij} = 0. \quad (4)$$

Subsequently, the pressure in pores is substituted into Eq. (3) to determine the flow rate q_{ij} in each throat. The total flow rate Q through the whole porous medium is obtained by summing the flow rates of all the throats connected to the inlet, like,

$$Q = \sum_{i \in \Omega_{in}} \sum_j |q_{ij}|, \quad (5)$$

where Ω_{in} represents the set of pores corresponding to the inlet. The absolute permeability is calculated as

$$K = \frac{Q\mu L}{A_0 \Delta P}, \quad (6)$$

where A_0 and L are the cross-sectional area and the length of the porous medium, respectively.

To demonstrate the reliability of the present model for fluid flow, we compare the relative errors in the absolute permeability predicted by the present model with those predicted by models based on other methods for pore-throat segmentation. Fig. 2 compares the relative errors in the predicted absolute permeability among different pore network models, with samples encompassing sand pack, sandstone, and carbonate. The relative error is defined as $((K_x^p + K_y^p + K_z^p) - (K_x^L + K_y^L + K_z^L))/(K_x^L + K_y^L + K_z^L)$, where K_x^p , K_y^p , and K_z^p denote the absolute permeability along the x , y , and z directions of the media, as predicted by pore network models, while K_x^L , K_y^L , and K_z^L represent the exact values by LBM simulations. The LBM simulations have been described and completed in our previous work and the permeability data are cited from the same source (Liu et al., 2022). The present model outperforms other models in predicting flow in porous media, with an average relative error of only 5.4 % in the predicted absolute permeability.

2.2. Network model for mass transfer

Solute transport in porous media is governed by the mass balance in all network elements, including pores and throats. The transport of chemical species takes place by advection and diffusion mechanisms.

Firstly, we formulate the governing equations of mass transfer in the present model. To illustrate, we consider a specific pore denoted as i , as

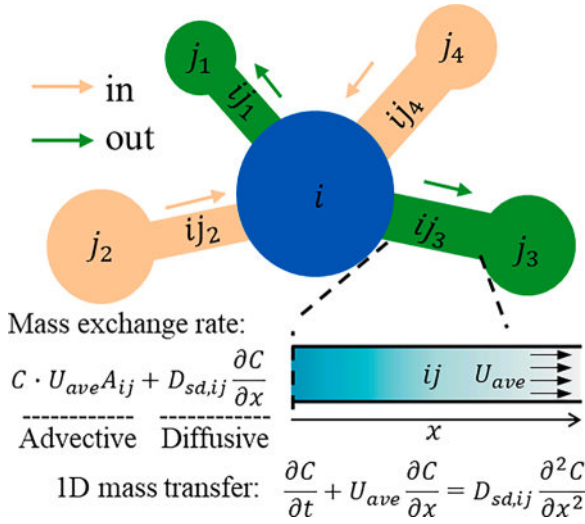


Fig. 3. Schematic of fluid flow and mass transfer between pores and throats.

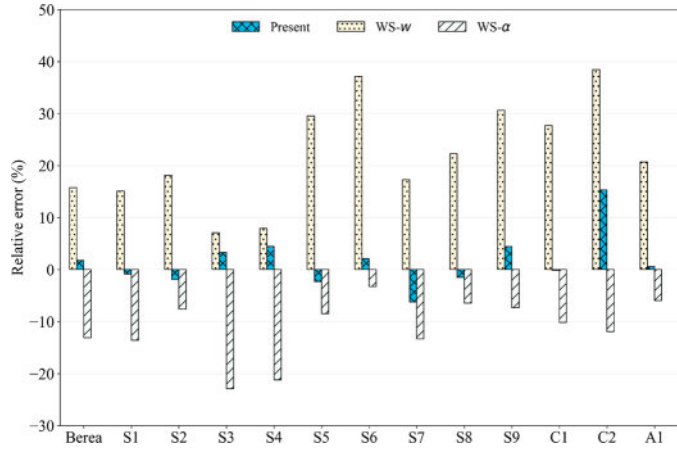


Fig. 4. The relative errors in the predicted formation factor by different models. ‘Present’ stands for the results predicted by the present model. ‘WS – w’, and ‘WS – α ’ denote the results predicted by the models where the w method (Liu et al., 2022; Sholokhova et al., 2009) and the α method (Liu et al., 2022; Øren and Bakke, 2003; Dong and Blunt, 2009) are used for pore-throat segmentation. Samples include sandstone (Berea and S1-S9), carbonate (C1-C2), and sand pack (A1) (Dong and Blunt, 2009).

shown in Fig. 3. The x^{th} neighboring pore of pore i is denoted as j_x and the connecting throat is denoted as ij_x . We use C_i , V_i , and l_i to represent the concentration, the volume, and the diffusive conduit length of pore i , respectively. The corresponding quantities for throat ij are denoted with a similar notation but with the subscript i changed to ij . It is important to note that the hydraulic conduit length for the calculation of hydraulic conductance in Eq. (1) differs from the diffusive conduit length described here. The former is determined by the local hydraulic resistance, which is inversely proportional to the fourth power of the radii, while the latter is determined by the local diffusive resistance, which is inversely proportional to the second power of the radii.

To reproduce the pore-scale shear dispersion effect, the present model incorporates pore-scale shear dispersion coefficients, denoted as $D_{sd,i}$ and $D_{sd,ij}$, to calculate the diffusive mass exchange rate between network elements in the simulation of mass transfer (see Fig. 3). These coefficients are locally determined through the application of the extension of Taylor-Aris theory, namely, Eq. (17), which will be introduced at length in Section 2.3. The pore-scale shear dispersion coefficient is a function of the local flow time t and local Péclet number Pe .

More specifically, t represents the advection time of the fluid within a network element (a pore or throat), i.e., the time required to move from the inlet to the outlet at the average velocity. The local flow time is calculated as $t = \frac{l}{U_{ave}}$, where l is the hydraulic conduit length of a network element and U_{ave} represents the average velocity within it. The average velocity is defined as $U_{ave} = \frac{q_{ij}}{A}$, where A represent the cross-sectional area of a pore or throat. The local Péclet number is defined as $Pe = \frac{U_{ave}R}{D_m}$, where R is the radius of a network element. Due to variations in geometry and flow conditions, the local flow time t and local Péclet number Pe can significantly differ among different pores or throats, ultimately leading to distinct local shear dispersion coefficient within each pore or throat. It is especially important to emphasize that the flow time t signifies a local flow characteristic and should not be confused with the evolution time of solute transport. In this study, steady state flow is assumed, and therefore the local shear dispersion coefficient does not change with the evolution time.

For the control volume of pore i , the mass balance equation can be expressed as follows:

$$V_i \frac{dC_i}{dt} = \sum_{in} q_{ij} \cdot C_{ij} - \sum_{out} q_{ij} \cdot C_i + \sum_j \frac{C_{ij} - C_i}{\frac{l_i}{D_{sd,i}A_i} + \frac{0.5l_{ij}}{D_{sd,ij}A_{ij}}} \quad (7)$$

where the left-hand side term represents the net accumulation of mass within the control volume. The right-hand side terms, from left to right, correspond to the mass exchange due to advective inflow flux, advective outflow flux, and diffusive mass exchange rate, respectively.

Similarly, the mass balance equation for the control volume of throat ij is given by:

$$V_{ij} \frac{dC_{ij}}{dt} = q_{ij}(C_{in} - C_{out}) + \frac{C_i - C_{ij}}{\frac{l_i}{D_{sd,i}A_i} + \frac{0.5l_{ij}}{D_{sd,ij}A_{ij}}} + \frac{C_j - C_{ij}}{\frac{l_j}{D_{sd,j}A_j} + \frac{0.5l_{ij}}{D_{sd,ij}A_{ij}}} \quad (8)$$

where C_{in} and C_{out} are the concentration of pores flowing into and out of the throat ij , respectively. The implicit scheme is employed to solve the concentration field.

The reliability of the present model in simulating mass transfer is evaluated via cases involving diffusion through porous media under steady-state conditions. The setup of the cases are as follows: an initial concentration of zero within the porous medium is assumed, and the concentration at the inlet and outlet is maintained at unity and zero, respectively. Under steady-state conditions, molecular diffusion and electrical conduction within a porous medium share the same governing equation, i.e., the Laplace equation, along with identical boundary conditions, i.e., the Dirichlet boundary condition at both the inlet and outlet. Consequently, the solutions for these two processes exhibit similarity. Therefore, formation factor F , which characterizes the normalized electrical resistance of the pore structure, is utilized to validate the reliability of the pore network models.

Due to the similarity between Poiseuille’s law and Ohm’s law, pore network models compute the formation factor in a manner analogous to how permeability is determined. The electrical conductance of an individual network element is

$$g_e = \frac{A}{R_w l} \quad (9)$$

where A and l are the cross-sectional area and length in a pore or throat, respectively, and R_w is the water resistivity. The electrical conductance between pore i and pore j is determined as

$$g_{e,ij} = \frac{1}{\frac{1}{g_{ei}} + \frac{1}{g_{ej}} + \frac{1}{g_{ej}}} \quad (10)$$

and the electrical current is

$$q_{e,ij} = g_{e,ij}(\Phi_i - \Phi_j) \quad (11)$$

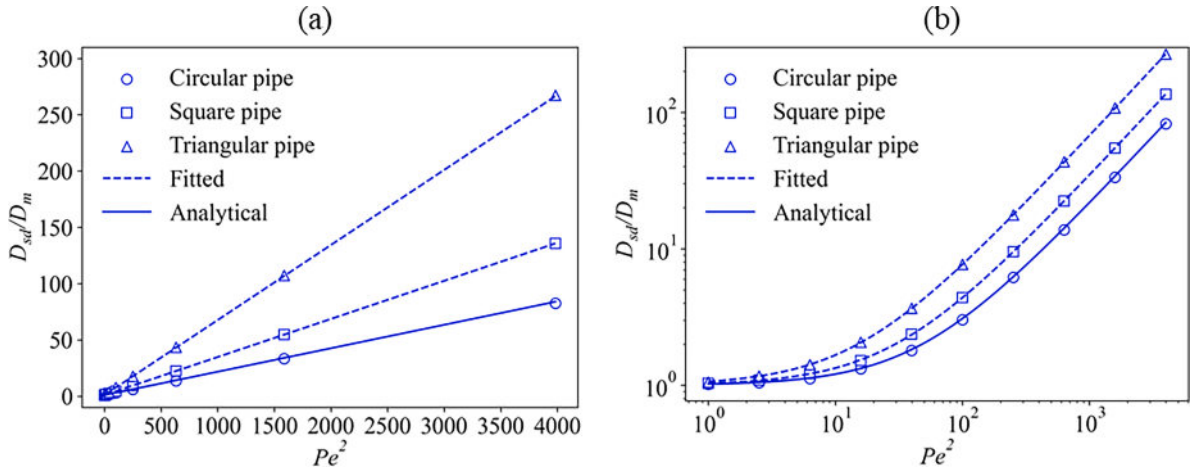


Fig. 5. Plot of the asymptotic shear dispersion coefficient D_{sd} versus Pe for pipes with different cross-sectional shapes: (a) linear plot and (b) log-log plot. Markers represent the results by random walk simulations and the dashed lines are fitted results. The solid line represents the Taylor-Aris analytical solution (Aris, 1956; Taylor, 1953) for shear dispersion in circular tubes.

Table 1

The fitted values of α and β for circular, square, and equilateral triangular pipes and the corresponding coefficient of determination r^2 .

Pipes	α	β	Coefficient of determination r^2
Circular pipes	1.0	15.0	1.00
Square pipes	1.0	10.8	1.00
Equilateral triangular pipes	1.0	4.8	0.99

where Φ_i and Φ_j denote the potential in pore i and pore j , respectively. With a potential difference of $\Delta\Phi$ between the inlet and outlet of the medium, the potential field is solved by imposing Kirchhoff's law at every pore. Consider pore i , for instance:

$$\sum_j q_{e,ij} = 0. \quad (12)$$

The total electrical current Q_e through the porous media is determined in a similar way as the determination of the total flow rate Q , and the formation factor is calculated as

$$F = \frac{A_0 \Delta\Phi}{Q_e R_w L}. \quad (13)$$

Fig. 4 compares the relative errors in the predicted formation factor among different pore network models, with samples encompassing sand pack, sandstone, and carbonate. The relative error is defined as $((F_x^p + F_y^p + F_z^p) - (F_x^e + F_y^e + F_z^e)) / (F_x^e + F_y^e + F_z^e)$, where F_x^p , F_y^p , and F_z^p denote the formation factor along the x , y , and z directions of the media, as predicted by pore network models, while F_x^e , F_y^e , and F_z^e represent the exact values determined by finite volume method (Yi et al., 2017). The present model yields significantly more accurate predictions compared to other models, exhibiting an average relative error of 3.5%.

2.3. Extension of Taylor-Aris theory

In this part, we provide an extension of Taylor-Aris theory, which plays a crucial role in enabling the present model to properly account for the pore-scale shear dispersion effect. Utilizing the extension of Taylor-Aris theory, we determine the pore-scale shear dispersion coefficients, $D_{sd,i}$ and $D_{sd,ij}$, thereby closing the set of equations presented in Section 2.2.

As mentioned in the background, the classical Taylor-Aris theory (Aris, 1956; Taylor, 1953) is invalid for porous media flow due to the finite lengths of network elements and the potential inability to reach

the asymptotic regime. To address this limitation, we conduct a comprehensive study on shear dispersion in pipes with circular, square, and equilateral triangular cross-sections using random walk simulations. By tracking the motion of a swarm of solute particles, we obtain the temporal variation of the shear dispersion coefficient and extend the classical Taylor-Aris theory (Aris, 1956; Taylor, 1953) to encompass the pre-asymptotic regime.

The random walk algorithm, employed in our simulations, is described in detail and rigorously validated in Appendix A. We study the shear dispersion in pipes with different cross-sections across a wide range of Péclet numbers. The Péclet number is defined as

$$Pe = \frac{U_{ave} R}{D_m}, \quad (14)$$

where R represents the inscribed radius of the pipe and U_{ave} denotes the average velocity of the pipe flow. The shear dispersion coefficient D_{sd} is determined by the variance of the tracers' longitudinal position, $\langle x^2 \rangle - \langle x \rangle^2$, and flow time t from the inlet, as

$$D_{sd} = \frac{1}{2} \frac{d(\langle x^2 \rangle - \langle x \rangle^2)}{dt} \approx \frac{1}{2} \frac{\Delta(\langle x^2 \rangle - \langle x \rangle^2)}{\Delta t}. \quad (15)$$

Fig. A.2(b) plots the shear dispersion coefficient D_{sd} as a function of flow time for circular pipes. The figure demonstrates the presence of two distinct regimes: the pre-asymptotic regime, characterized by an increasing trend of D_{sd} with flow time, and the asymptotic regime, where D_{sd} remains constant.

When the asymptotic regime is reached, the shear dispersion coefficient follows the Taylor-Aris theory (Aris, 1956; Taylor, 1953), given by:

$$\frac{D_{sd}}{D_m} = 1 + \kappa Pe^2, \quad (16)$$

where κ is a constant associated with the shape of pipe cross-sections. Utilizing the simulation results, the asymptotic shear dispersion coefficients were determined, and the values of κ for circular, square, and equilateral triangular pipes were fitted as 0.0208, 0.0338, and 0.0667, respectively. Remarkably, the fitted value of κ for circular pipes aligns perfectly with the analytical solution $\kappa = 1/48 \approx 0.0208$. Fig. 5 shows the plot of the asymptotic shear dispersion coefficient against Pe .

For the pre-asymptotic regime, the shear dispersion coefficient can be described by incorporating transient terms into Eq. (16) (Taghizadeh et al., 2020; Mauri and Haber, 1991). According to the work of Taghizadeh et al. (2020), these terms should exhibit exponential decay with flow time. Thus, we express the pre-asymptotic shear dispersion

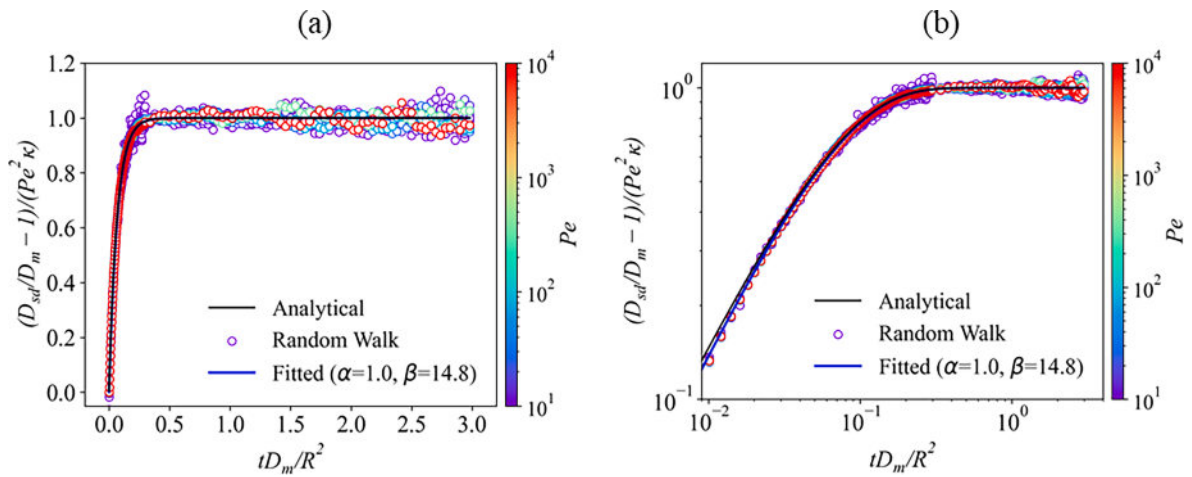


Fig. 6. Comparison of the pre-asymptotic shear dispersion coefficient D_{sd} for circular pipes, random walk simulations versus the fitted correlation, Eq. (17): (a) linear plot and (b) log-log plot. The analytical solution is presented by Taghizadeh et al. (2020).

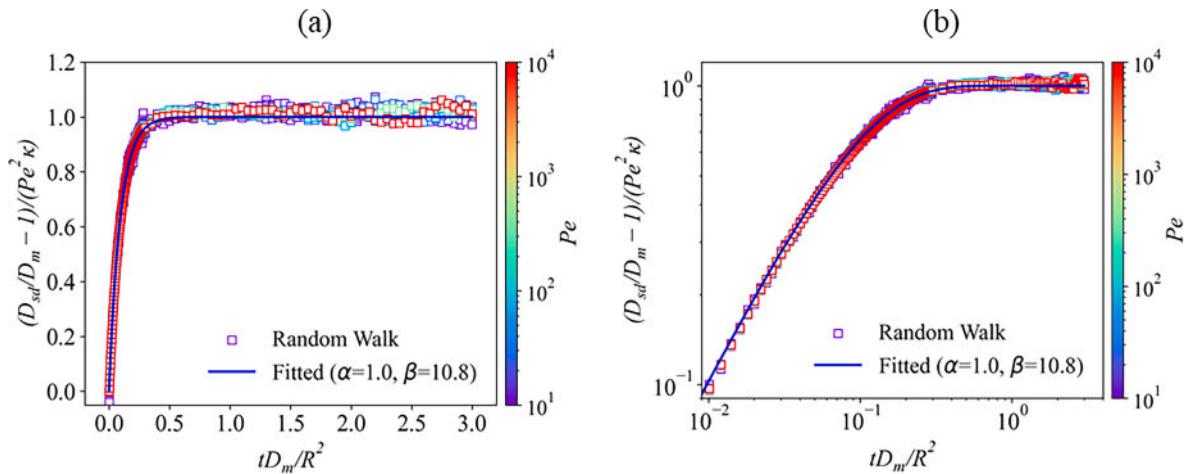


Fig. 7. Comparison of the pre-asymptotic shear dispersion coefficient D_{sd} for square pipes, random walk simulations versus the fitted correlation, Eq. (17): (a) linear plot and (b) log-log plot.

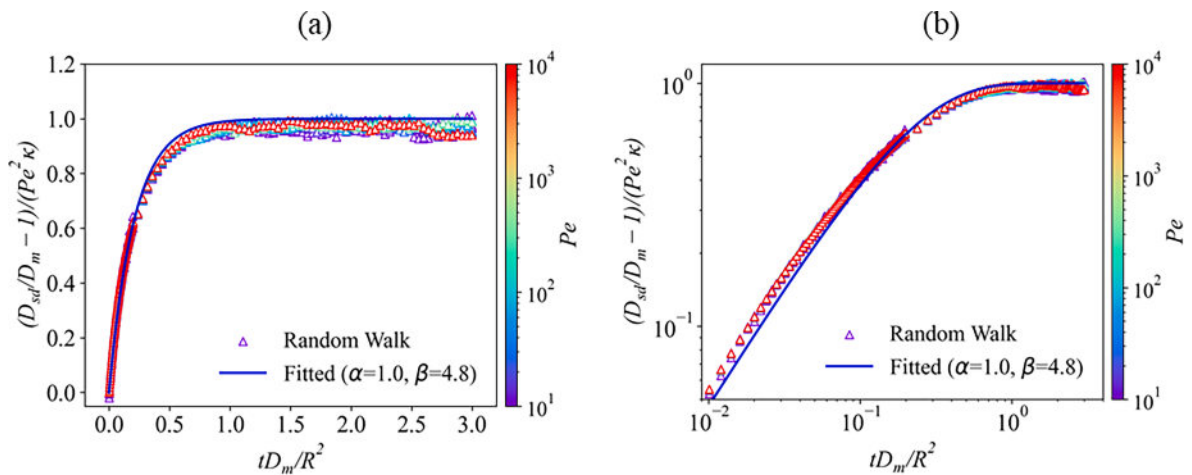


Fig. 8. Comparison of the pre-asymptotic shear dispersion coefficient D_{sd} for equilateral triangular pipes, random walk simulations versus the fitted correlation, Eq. (17): (a) linear plot and (b) log-log plot.

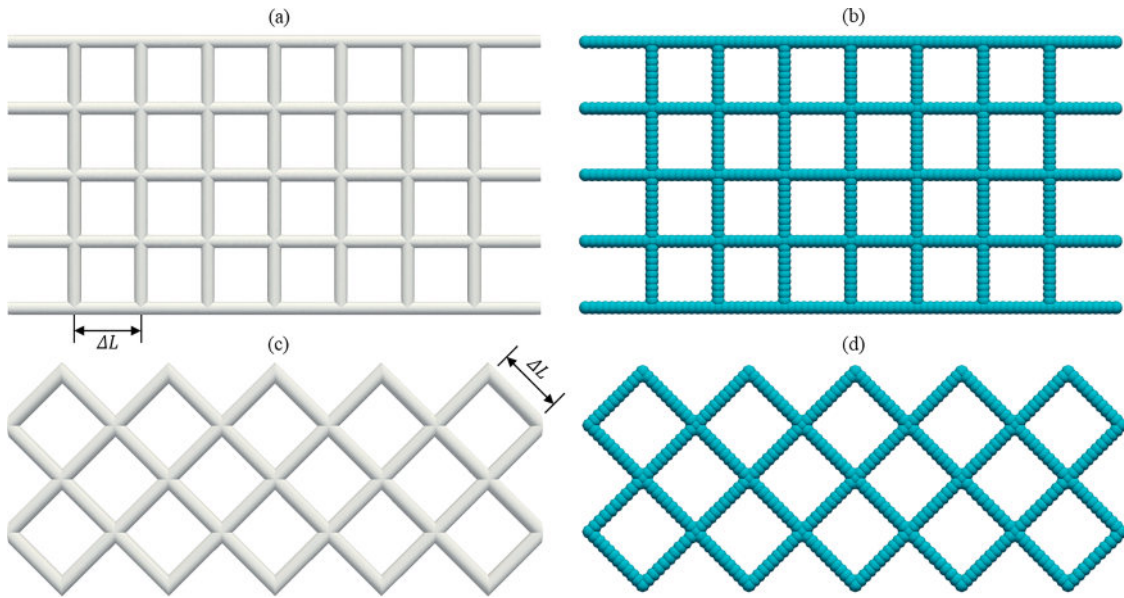


Fig. 9. Schematic of (left) tube networks and (right) the corresponding pore networks. (top) $TN - 90$ and (bottom) $TN - 45$.

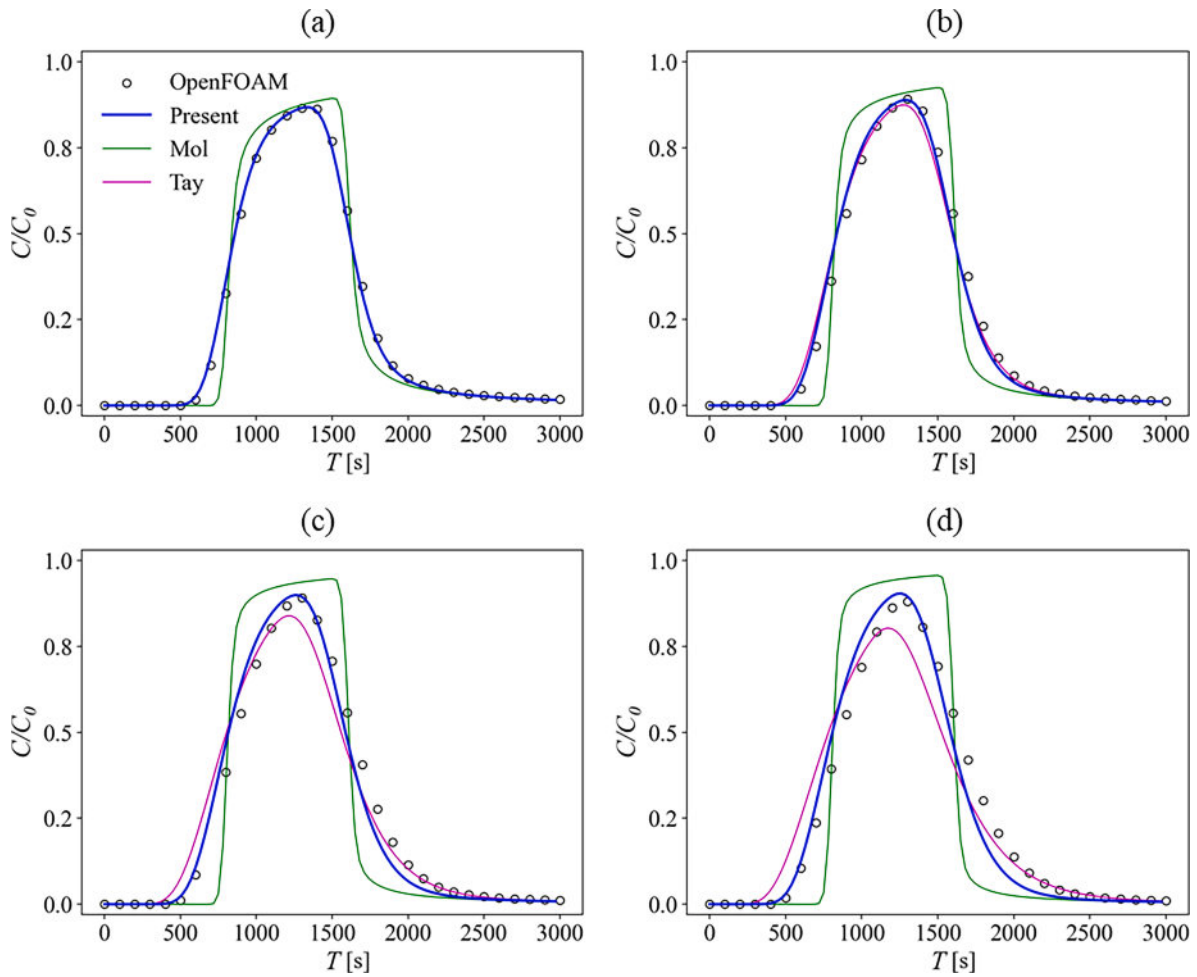


Fig. 10. Comparison of breakthrough curves of solute transport in $TN - 90$ at Pe_{TN} of (a) 50, (b) 100, (c) 200, and (d) 300. ‘Present’ stands for the results predicted by the present model. ‘Mol’ and ‘Tay’ represent the results predicted by the models that ignore pore-scale shear dispersion and invoke Taylor dispersion, respectively. ‘OpenFOAM’ denotes the DNS simulations. T denotes the evolution time from the start of the injection. ‘Present’ and ‘Tay’ are on top of each other and are indistinguishable in (a).

Table 2

The error metric E of different models for $TN - 90$ at Pe_{TN} of 50, 100, 200, and 300, respectively. 'Present' stands for the results predicted by the present model. 'Mol' and 'Tay' represent the results predicted by the models that ignore pore-scale shear dispersion and invoke Taylor dispersion, respectively.

Models	E (%)			
	$Pe_{TN} = 50$	$Pe_{TN} = 100$	$Pe_{TN} = 200$	$Pe_{TN} = 300$
'Present'	0.9	1.9	3.0	3.9
'Tay'	0.9	2.1	3.6	5.4
'Mol'	3.7	5.9	7.4	9.1

coefficient as the following form

$$\frac{D_{sd}/D_m - 1}{\kappa Pe^2} = 1 - \alpha \exp\left(-\beta \frac{D_m}{R^2} t\right), \quad (17)$$

where α and β are coefficients that depend on the shape of pipe cross-sections. The derivation and rationale behind Eq. (17) are extensively explained in Appendix B.

To determine the values of α and β , we perform fitting procedures based on the results obtained from random walk simulations. With the values of α and β in Table 1, the shear dispersion coefficient is determined based on Eq. (17) and is compared with the results of random walk simulations (see Figs. 6–8). By Eq. (17), we expand the classical Taylor-Aris theory (Aris, 1956; Taylor, 1953) to encompass the pre-asymptotic regime.

3. Validations

In this part, we validate the proposed model through cases with DNS solutions and experimental data. Additionally, we assess the accuracy of the other two categories of MCM-PNM. One category neglects the pore-scale shear dispersion effect, labeled as 'Mol', where the local diffusive flux is calculated solely based on the molecular diffusion coefficient. The other category invokes Taylor dispersion and is labeled as 'Tay', where the local diffusive flux is calculated based on the Taylor dispersion coefficient. The present model, labeled as 'Present', employs the extension of Taylor-Aris theory to properly account for the pore-scale shear dispersion effect, and the local diffusive flux is calculated based on the pore-scale shear dispersion coefficient. To quantitatively assess the accuracy of predictions by different models for solute transport, we

Table 3

The error metric E of different models for $TN - 45$ at Pe_{TN} of 25, 100, 300, and 500, respectively. 'Present' stands for the results predicted by the present model. 'Mol' and 'Tay' represent the results predicted by the models that ignore pore-scale shear dispersion and invoke Taylor dispersion, respectively.

Models	E (%)			
	$Pe_{TN} = 25$	$Pe_{TN} = 100$	$Pe_{TN} = 300$	$Pe_{TN} = 500$
'Present'	3.7	3.2	2.6	3.0
'Tay'	3.7	3.2	4.4	6.2
'Mol'	4.6	8.1	11.0	13.0

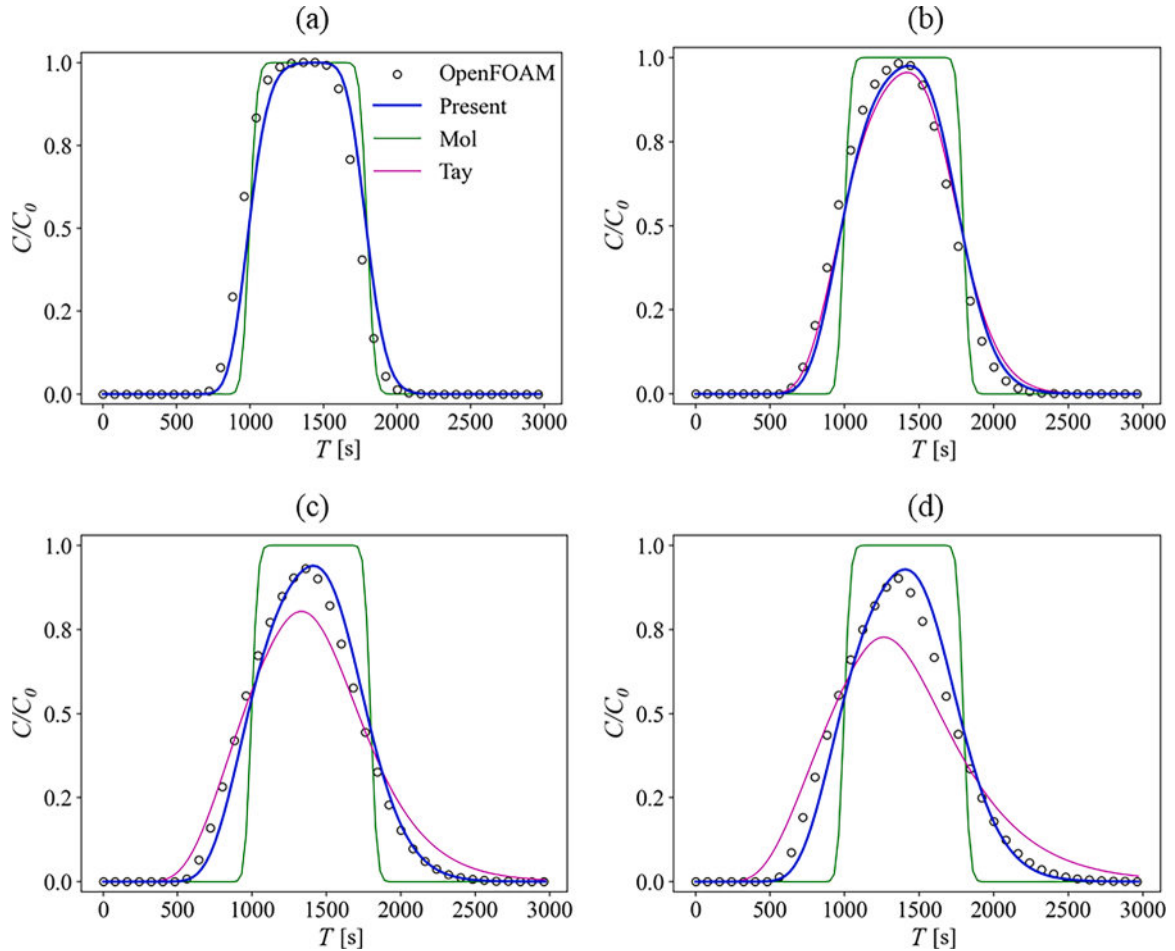


Fig. 11. Comparison of breakthrough curves of solute transport in $TN - 45$ at Pe_{TN} of (a) 25, (b) 100, (c) 300, and (d) 500. 'Present' stands for the results predicted by the present model. 'Mol' and 'Tay' represent the results predicted by the models that ignore pore-scale shear dispersion and invoke Taylor dispersion, respectively. 'OpenFOAM' denotes the numerical simulation results. T denotes the evolution time from the start of the injection. 'Present' and 'Tay' are on top of each other and are indistinguishable in (a).

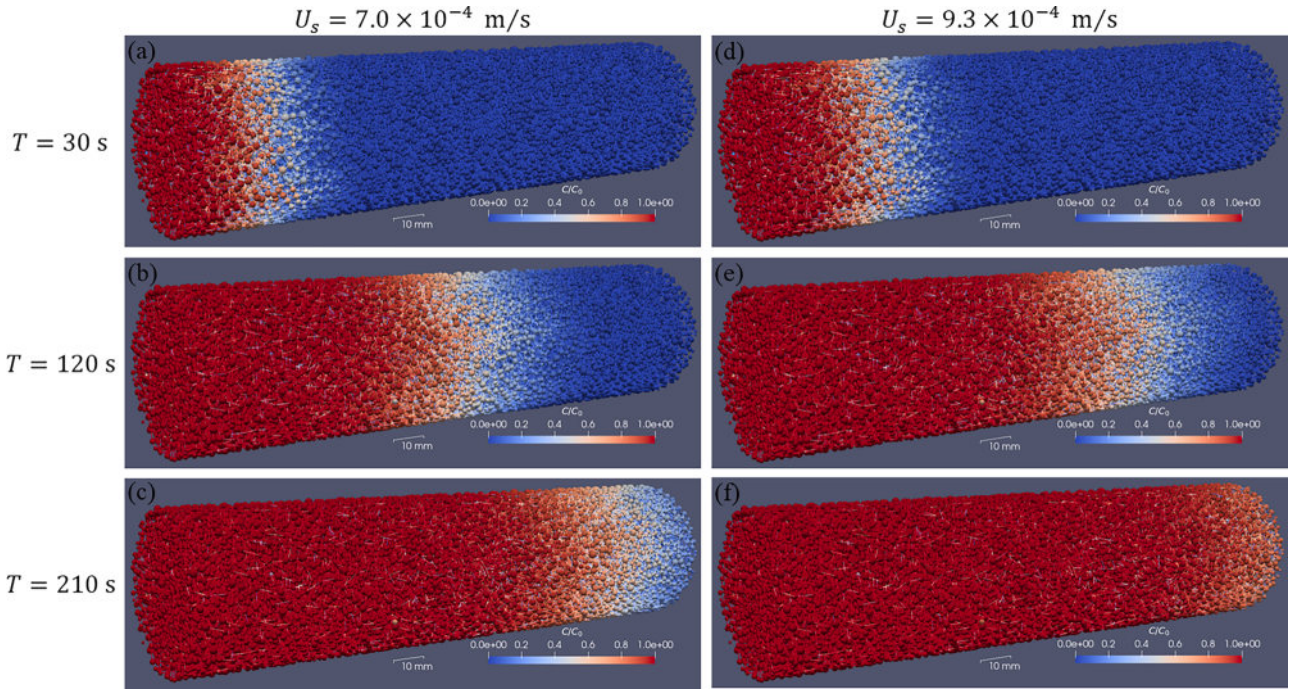


Fig. 12. The temporal evolution of solute concentration in the bead pack predicted by the present model, (left) $U_s = 7.0 \times 10^{-4}$ m/s and (right) $U_s = 9.3 \times 10^{-4}$ m/s. The top row, middle row, and bottom row correspond to evolution times T of 30s, 120s, 210s, respectively, from the start of the injection.

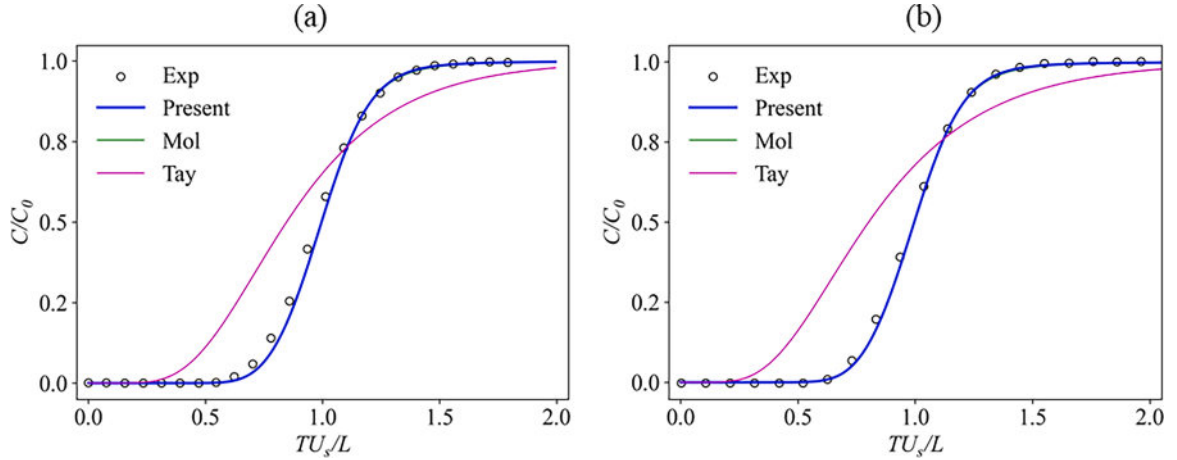


Fig. 13. Comparison of breakthrough curves of solute transport in the bead pack for (a) $U_s = 7.0 \times 10^{-4}$ m/s and (b) $U_s = 9.3 \times 10^{-4}$ m/s. U_s is the seepage velocity, T denotes the evolution time from the start of the injection, and $L=180$ mm is the column length. ‘Present’ stands for the results predicted by the present model. ‘Mol’ and ‘Tay’ represent the results predicted by the models that ignore pore-scale shear dispersion and invoke Taylor dispersion, respectively. ‘Exp’ is the experimental data by Raje and Kapoor (2000). ‘Present’ and ‘Mol’ are on top of each other and are indistinguishable.

Table 4

The error metric E of different models for the bead pack at U_s of 7.0×10^{-4} m/s and 9.3×10^{-4} m/s. ‘Present’ stands for the results predicted by the present model. ‘Mol’ and ‘Tay’ represent the results predicted by the models that ignore pore-scale shear dispersion and invoke Taylor dispersion, respectively.

Models	E (%)	
	$U_s = 7.0 \times 10^{-4}$ m/s	$U_s = 9.3 \times 10^{-4}$ m/s
‘Present’	1.2	0.8
‘Tay’	9.2	11.0
‘Mol’	1.2	0.8

introduce an error metric, which is defined as

$$E = \frac{\sum_{i \leq N_0} |C_i^{ref} - C_i^{PNM}|}{N_0} \times 100\%, \quad (18)$$

where C_i^{ref} represents the i^{th} value of breakthrough curves or concentration profiles in the reference dataset (experimental data or numerical results) with the total number of N_0 . C_i^{PNM} represents data by linearly interpolating the predictions of pore network models at the same time or location as the reference dataset. A smaller value of E indicates that the prediction is closer to the reference dataset.

3.1. Case I: solute transport in tube networks

The first case involves solute transport in tube networks. Two types

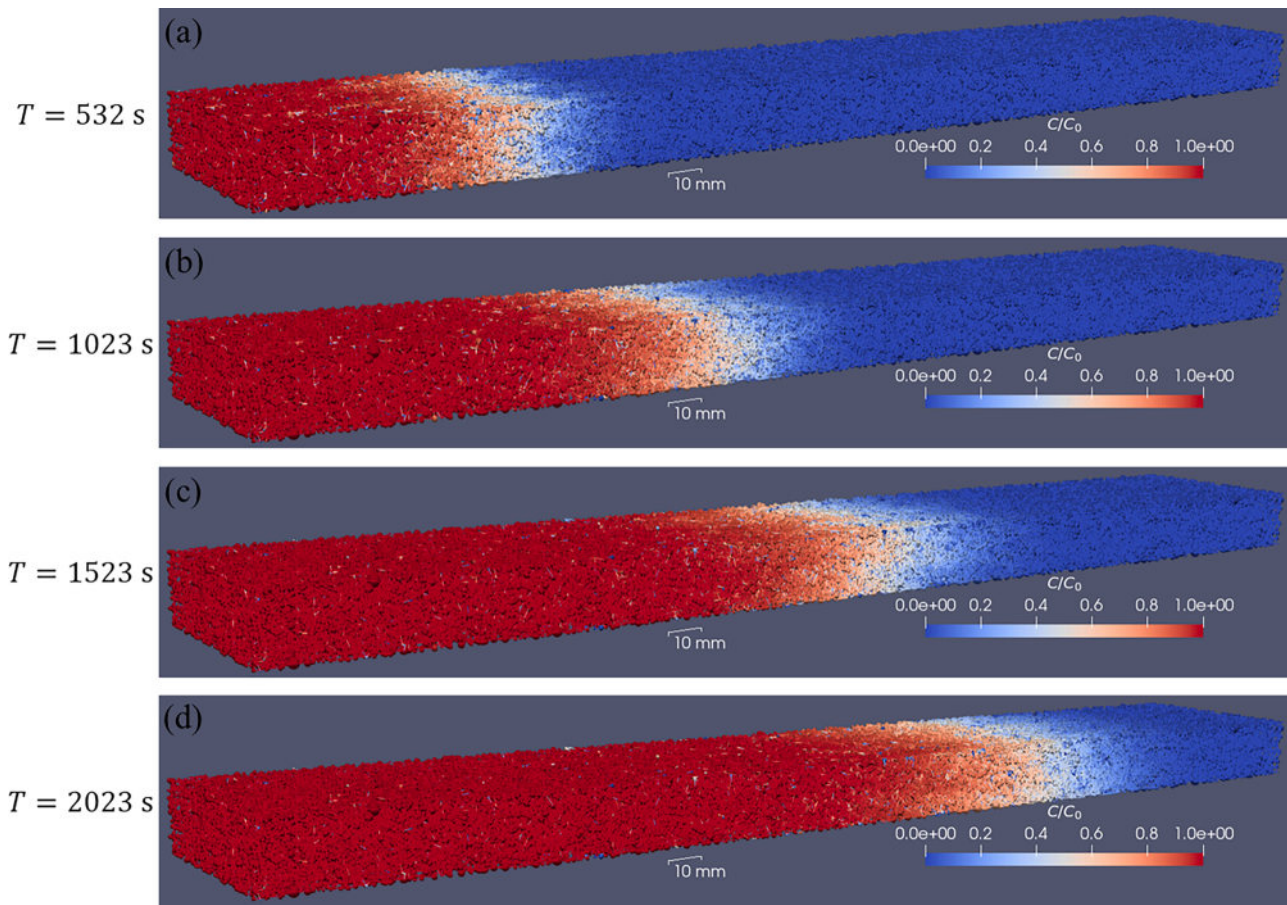


Fig. 14. The temporal evolution of solute concentration in the sand pack predicted by the present model. From top to bottom, the evolution times T are 532s, 1023s, 1523s, and 2023s, respectively.

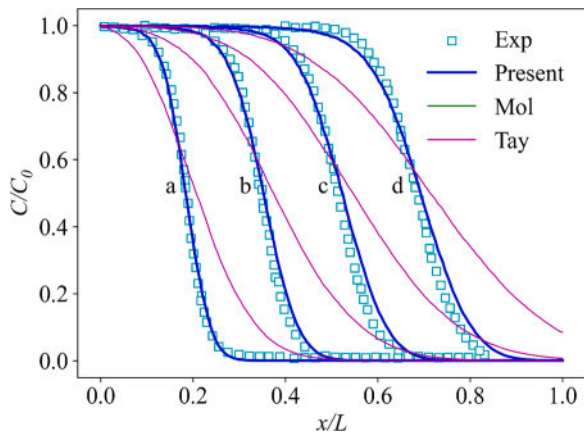


Fig. 15. Comparison of concentration profiles of solute transport in the sand pack. a, b, c, and d correspond to evolution times T of 532s, 1023s, 1523s, and 2023s, respectively. x is the location along the flow direction and L is the column length. ‘Present’ stands for the results predicted by the present model. ‘Mol’ and ‘Tay’ represent the results predicted by the models that ignore pore-scale shear dispersion and invoke Taylor dispersion, respectively. ‘Exp’ is the experimental data by Gramling et al. (2002). ‘Present’ and ‘Mol’ are on top of each other and are indistinguishable.

of tube networks, namely $TN - 90$ and $TN - 45$, are considered, where the tubes are aligned at angles of 90° and 45° to the mainstream, respectively. Both and $TN - 45$ have a tube radius R of 0.001m and an alignment space ΔL of 0.01m. Fig. 9 demonstrates the geometry of the

Table 5

The error metric E of different models for the sand pack at evolution times T of 532s, 1023s, 1523s, and 2023s, respectively. ‘Present’ stands for the results predicted by the present model. ‘Mol’ and ‘Tay’ represent the results predicted by the models that ignore pore-scale shear dispersion and invoke Taylor dispersion, respectively.

Models	E (%)			
	$T = 532 \text{ s}$	$T = 1023 \text{ s}$	$T = 1523 \text{ s}$	$T = 2023 \text{ s}$
‘Present’	1.9	2.6	3.2	3.8
‘Tay’	12.0	13.0	14.0	15.0
‘Mol’	1.9	2.6	3.2	3.8

tube networks and the corresponding pore networks, with the mainstream from left to right. For $TN - 90$, a constant injection rate of $1.57 \times 10^{-9} \text{ m}^3/\text{s}$ is applied, resulting in an average velocity U_{ave} of $1.00 \times 10^{-4} \text{ m/s}$. Similarly, for $TN - 45$, a constant injection rate of $1.26 \times 10^{-9} \text{ m}^3/\text{s}$ is used, corresponding to an average velocity U_{ave} of $1.00 \times 10^{-4} \text{ m/s}$. At the inlet, a solute pulse with a concentration of C_0 is introduced, while the concentration is assumed to be fully developed at the outflow, i.e., zero concentration gradient along the flow direction. The pulse duration t_p is set to 800s for both $TN - 90$ and $TN - 45$. Refined segments are introduced between tube intersections to improve accuracy, where the tube length of ΔL is further subdivided into 100 refined segments. The local flow time t in Eq. (17) is calculated by dividing the alignment space ΔL by the local average velocity U_{ave} . Here, the Péclet number is defined as $Pe_{TN} = U_{ave}R/D_m$, where D_m is the molecular diffusion coefficient. By varying D_m , the solute transport at different Pe_{TN} is examined. DNS solutions are obtained using the open-source

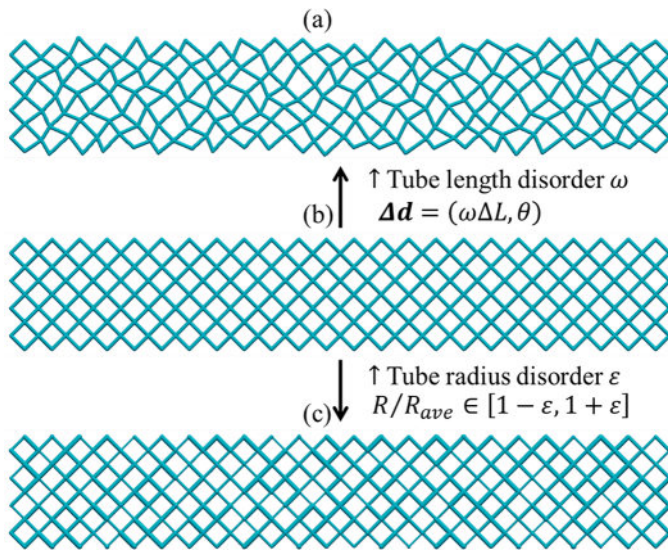


Fig. 16. Schematic of (b) the base tube network and the tube networks with different (a) tube length disorder ω and (c) tube radius disorder ε . Δd denotes the vector of movement of tube intersections with the length of $\omega\Delta L$ and the direction of θ in a polar coordinate. ΔL is the alignment space and θ is randomly distributed in the range of $[0, 2\pi]$. R_{ave} is the average tube radius with a value of 0.001m.

software, OpenFOAM. The detailed setup for the OpenFOAM simulations can be found in Appendix C.

For $TN = 90$, solute transport is modeled at $Pe_{TN} = 50, 100, 200$, and 300. The present model exhibits good agreement with the direct numerical simulation results (see Fig. 10). The model that ignores pore-scale shear dispersion, namely, ‘Mol’, significantly deviates from the direct numerical simulation results for all Pe_{TN} . The model that invokes Taylor dispersion, namely, ‘Tay’, agrees well with the numerical simulation results at low Pe_{TN} , but it exhibits large errors at high Pe_{TN} . The error in predictions of different models is quantitatively assessed via the error metric E, which is given in Table 2. At different Pe_{TN} , ‘Present’ exhibits the smallest error, whereas ‘Mol’ shows the highest error. As the Pe_{TN} increases, the error for ‘Tay’ increases.

For $TN = 45$, solute transport is modeled at $Pe_{TN} = 25, 100, 300$, and 500. In Fig. 11, the breakthrough curves predicted by pore network models are compared with the numerical simulation results. The error in predictions of different models is given in Table 3. Once again, the present model provides much more accurate predictions than the other two models.

3.2. Case II: solute transport in the bead pack

In the second case, we simulate the experiments by Raje and Kapoor (2000). With the same bead size (diameter $g = 3\text{mm}$) and column size (length $L = 180\text{mm}$, diameter $d_0 = 45\text{mm}$) as the experimental bead pack, the pore structure is reconstructed using the *pseudo_gravity_packing* module in Porespy (Gostick, 2017). Fig. D1(a, c) displays the pore size distribution and conduit length distribution of the reconstructed porous medium. The reconstructed porous medium has a porosity of 0.45, identical to that of the column in the experiments. The molecular diffusion coefficient D_m is $4.6 \times 10^{-10}\text{m}^2/\text{s}$. Two cases are modeled with seepage velocities U_s of $7.0 \times 10^{-4}\text{m/s}$ and $9.3 \times 10^{-4}\text{m/s}$, corresponding to $Pe = U_s g / D_m$ of 4565 and 6065, respectively. A constant concentration of C_0 is maintained at the inlet, while a fully developed concentration is assumed at the outlet, i.e., zero concentration gradient along the flow direction.

The pore network consists of 32,796 pores and 129,770 throats, and the present model takes about 3 min to complete a simulation case. However, as reported by Mehmani et al. (Mehmani and Balhoff, 2015),

the superposing transport method necessitates several hours to complete a case where the pore network is composed of 4094 pores and 10,184 throats. Thus, the present model demonstrates a substantially improved computational efficiency compared to the superposing transport method.

Fig. 12 shows the temporal evolution of solute concentration during transport in the bead pack. The breakthrough curves predicted by the present model and the model that ignores pore-scale shear dispersion show good agreement with the experimental data (see Fig. 13). However, the model that invokes Taylor dispersion produces breakthrough curves that exhibit much higher diffusivity than the experimental data. This overestimated diffusivity is attributed to the utilization of Taylor dispersion, which overestimates the pore-scale shear dispersion effect. A quantitative comparison of errors in the prediction by different models is presented in Table 4. Both ‘Present’ and ‘Mol’ demonstrate remarkably low errors in prediction, with their values nearly identical. In contrast, ‘Tay’ exhibits a notably high error in prediction.

3.3. Case III: solute transport in the sand pack

The present model is further validated using experimental data on solute transport in a sand pack (Gramling et al., 2002). The sand pack is represented by a random pack of monodisperse spheres with the same average grain size (diameter $g = 1.3\text{mm}$) and domain size (length $L = 360\text{mm}$, width $W = 55\text{mm}$, and height $H = 18\text{mm}$). The structure generation is performed using the *pseudo_gravity_packing* module in Porespy (Wang et al., 2020). Fig. D1 (b, d) presents the pore size distribution and conduit length distribution of the reconstructed porous medium. The generated sphere pack has a porosity of 0.36, identical to that of the sand pack in the experiment. The molecular diffusion coefficient D_m is $7.02 \times 10^{-11}\text{m}^2/\text{s}$. The injection rate is set at 2.67mL/min, and the corresponding seepage velocity U_s is $1.21 \times 10^{-4}\text{m/s}$, resulting in $Pe = U_s g / D_m$ of 2240. A constant concentration of C_0 is maintained at the inlet, and a remote boundary condition is assumed for the outflow.

Fig. 14 displays the temporal evolution of solute concentration during transport in the sand pack. The concentration profiles at evolution times T of 532s, 1023s, 1523s, and 2023s are predicted by the pore network models and compared with the experimental data in Fig. 15. The concentration profiles predicted by the present model and the model that ignores pore-scale shear dispersion demonstrate good agreement with the experimental data. However, the incorporation of Taylor dispersion results in significant deviations between the predicted results and the experimental data. The huge error is attributed to the utilization of Taylor dispersion, which overestimates the pore-scale shear dispersion effect. A quantitative comparison of the errors in prediction of different models is presented in Table 5. The errors in prediction by both ‘Present’ and ‘Mol’ are small and their values are almost the same. In contrast, the error in prediction by ‘Tay’ is significantly higher.

4. The impact of geometrical disorder

An interesting observation in Section 3 is that the difference between ‘Present’ and ‘Mol’ is dramatic in tube networks but negligible in disordered media, such as the bead pack and the sand pack. This finding suggests that the impact of pore-scale shear dispersion on solute transport varies across different types of porous media.

In this section, we explore the structural factors that influence the significance of pore-scale shear dispersion on solute transport, with a specific focus on the effect of geometrical disorder. To begin, we establish a base tube network composed of pipes with uniform radii of 0.001m. These pipes are aligned at an angle of 45° to the mainstream, with an alignment space ΔL of 0.01m and 9×25 intersections (see Fig. 16(b)). Next, we introduce variations in locations of tube intersections and tube radii to examine the impact of tube length disorder and tube radius disorder, respectively (see Fig. 16(a) and 16(c)). Tube radius disorder is quantified by the parameter ε , which indicates that the

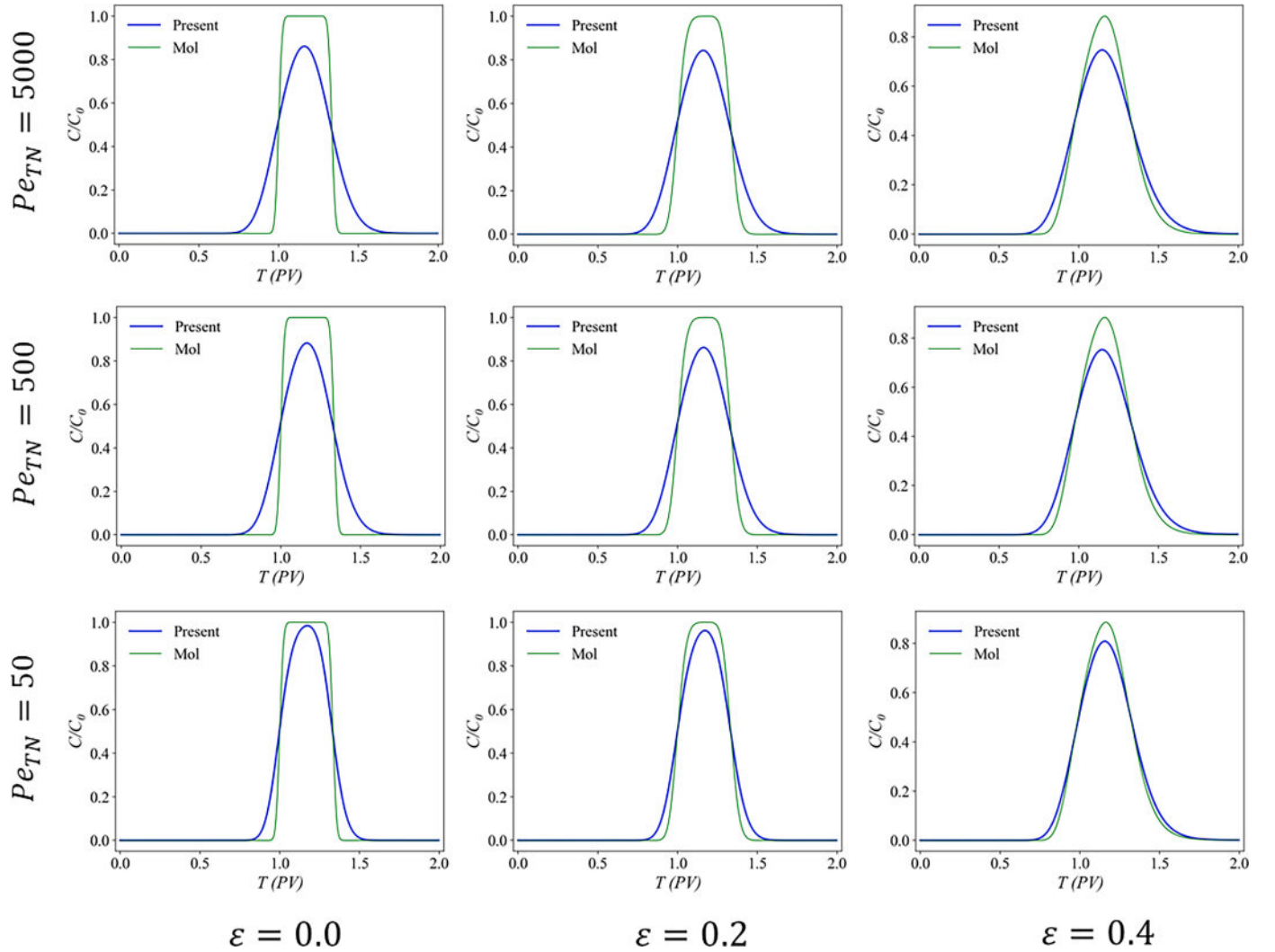


Fig. 17. Comparison of breakthrough curves for different Pe_{TN} and tube radius disorder ε . ‘Present’ and ‘Mol’ denote the results predicted by the present model and the model ignores pore-scale shear dispersion, respectively.

tube radii are uniformly distributed in $[1 - \varepsilon, 1 + \varepsilon] \times R_{ave}$, where R_{ave} represents the average radius of 0.001m (see Fig. 16(c)). On the other hand, tube length disorder is characterized by the parameter ω , which represents the displacement of intersection nodes by $\omega\Delta L$ in random directions (see Fig. 16(a)). Larger values of ε or ω correspond to a stronger degree of disorder in tube radius or tube length, respectively.

We simulate solute transport in tube networks with varying values of ε or ω at different injection rates Q_{inj} . At the inlet, a solute pulse with a concentration of C_0 is introduced, while the outflow is assumed to reach a fully developed concentration. The duration of the pulse, t_p , is set to

$$t_p = PV/3, \quad (19)$$

where PV is the time required to inject one pore volume.

The Péclet number is defined as $Pe_{TN} = U_{ave}R_{ave}/D_m$, where $U_{ave} = Q_{inj}/9\pi R_{ave}^2$. We compare the breakthrough curves predicted by the present model with those obtained from the model that ignores pore-scale shear dispersion in Figs. 17–19. We define a parameter χ to characterize the temporal width of the breakthrough curves, as:

$$M_1 = \frac{\int T \cdot CdT}{\int CdT}, \quad (20)$$

$$M_2 = \frac{\int T^2 \cdot CdT}{\int CdT}, \quad (21)$$

$$\chi = M_2 - M_1^2, \quad (22)$$

where C is the average concentration at the outlet and T is the evolution time normalized by PV . A larger value of χ indicates the enhanced overall dispersion. Hence, we evaluate the impact of pore-scale shear dispersion on solute transport via $\chi_{present}/\chi_{Mol}$, where $\chi_{present}$ and χ_{Mol} are calculated based on the breakthrough curves predicted by the present model and the model that ignores pore-scale shear dispersion, respectively.

Fig. 20 illustrates the influence of tube radius disorder ε and tube length disorder ω on $\chi_{present}/\chi_{Mol}$ at various Pe_{TN} . $\chi_{present}/\chi_{Mol}$ decreases with ε and ω over a wide range of Pe_{TN} , indicating that the impact of pore-scale shear dispersion on solute transport weakens for tube networks with increasing degrees of geometrical disorder. Regarding the mechanisms of the weakening of shear dispersion effect, our recent progress suggests that this may arise from alterations in the flow field or changes in the local shear dispersion coefficients, which are caused by an increase in geometrical disorder. This issue will be explored in depth in our next work.

The pore size distribution and conduit length distribution in both the bead pack and sand pack exhibit a high degree of geometrical disorder (see Fig. D.1), which implies negligible impact of shear dispersion, further explaining the overlap between ‘Mol’ and ‘Present’ in Sections 3.2 and 3.3. On the other hand, as Pe increases, the error in prediction by

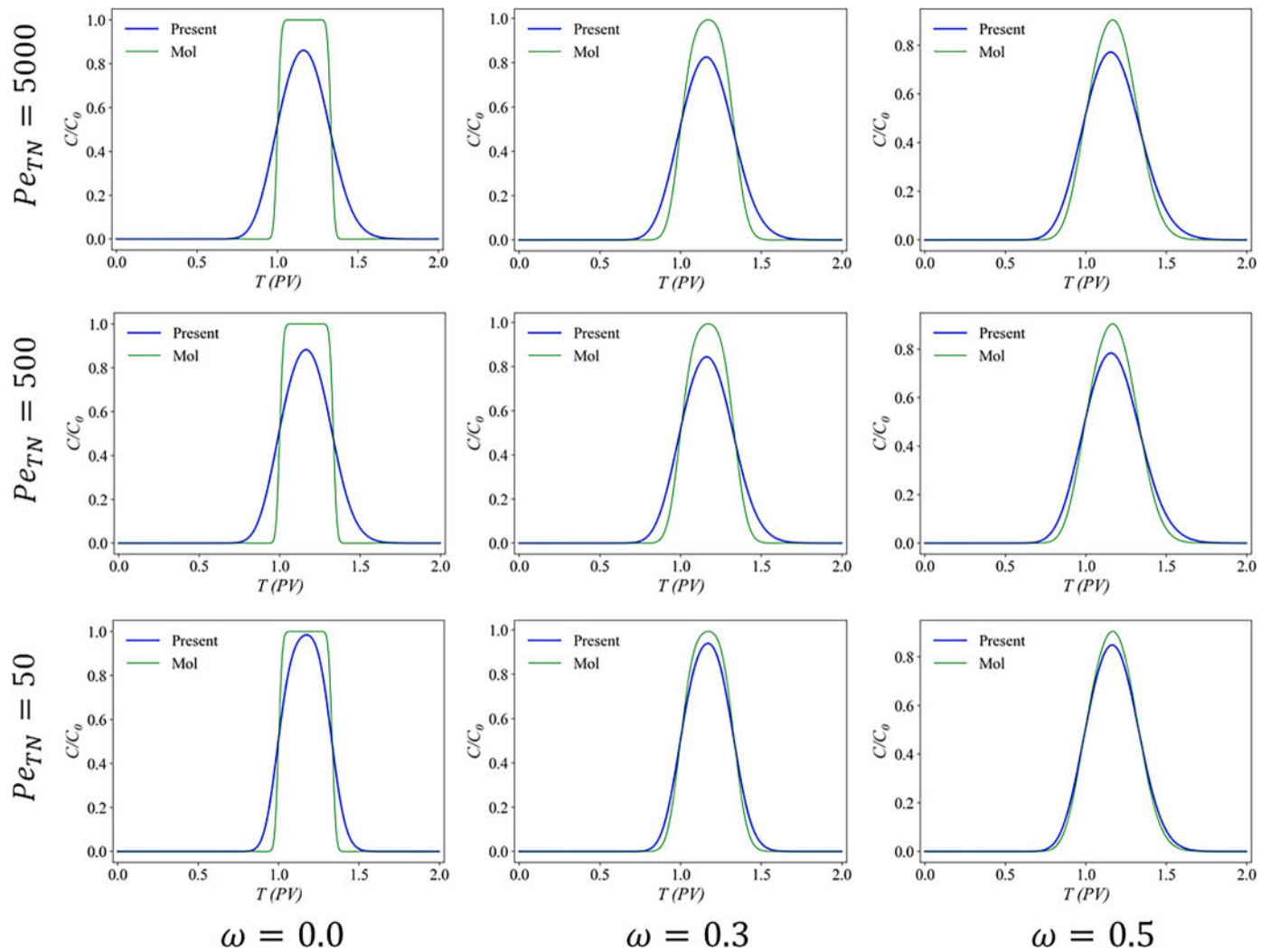


Fig. 18. Comparison of breakthrough curves for different Pe_{TN} and tube length disorder ω . ‘Present’ and ‘Mol’ denote the results predicted by the present model and the model ignores pore-scale shear dispersion, respectively.

‘Tay’ increases (see Tables 2–4, Figs. 10 and 11). This is due to the fact that the finite length effect of flow channels becomes more pronounced as the Pe increases, which implies that the discrepancy between Taylor dispersion and the actual pre-asymptotic dispersion becomes more significant. In the two cases presented in Sections 3.2 and 3.3, the Péclet numbers Pe are as high as 6065 and 2240, respectively. Therefore, in such situations, the utilization of Taylor dispersion to approximate actual shear dispersion introduces a significant error. This accounts for the substantial deviation of predictions by ‘Tay’ from the experimental results in Sections 3.2 and 3.3. Both $TN = 90$ and $TN = 45$ are highly ordered structures, characterized by uniform tube diameter and tube length. In this scenario, shear dispersion exerts a significant influence on solute transport, which explains the significant errors in predictions by ‘Mol’. Nevertheless, at small Pe , ‘Tay’ restores shear dispersion effects to some extent, making ‘Tay’ more accurate than ‘Mol’ in tube network cases.

5. Conclusions

We have proposed a pore network framework for solute transport and dispersion in porous media, which ensures both accuracy and efficiency. The proposed model incorporates the pore-scale shear dispersion effect by utilizing the pore-scale shear dispersion coefficient to calculate the diffusive mass exchange rate between network elements. The

determination of this coefficient is based on the extension of the classical Taylor-Aris theory to encompass the pre-asymptotic regime. In our model, both pores and throats contribute to the resistance and volumes, and conduit lengths and volumes of the network elements are determined from the equivalence of local resistance (Liu et al., 2022). To validate our model, we conducted a series of testing cases, including direct simulation results and experimental data. The present model provides good predictions for all the testing cases investigated in this paper, while the other two models, i.e., neglecting pore-scale shear dispersion or relying on Taylor dispersion, may lead to significant errors in simulation outcomes. We further illustrate that the impact of pore-scale shear dispersion on solute transport weakens for tube networks with increasing degrees of geometrical disorder. This finding explains the observation that the difference between our new model and the model that neglects pore-scale shear dispersion is significant for solute transport in regular tube networks but negligible for solute transport in disordered porous media, such as bead pack and sand pack. The transition can be attributed to the small geometrical disorder of regular tube networks but a much larger geometrical disorder in the bead pack and the sand pack. Future research efforts will focus on applying the proposed model to study solute transport in real porous materials, further enhancing our understanding of transport phenomena in these systems.

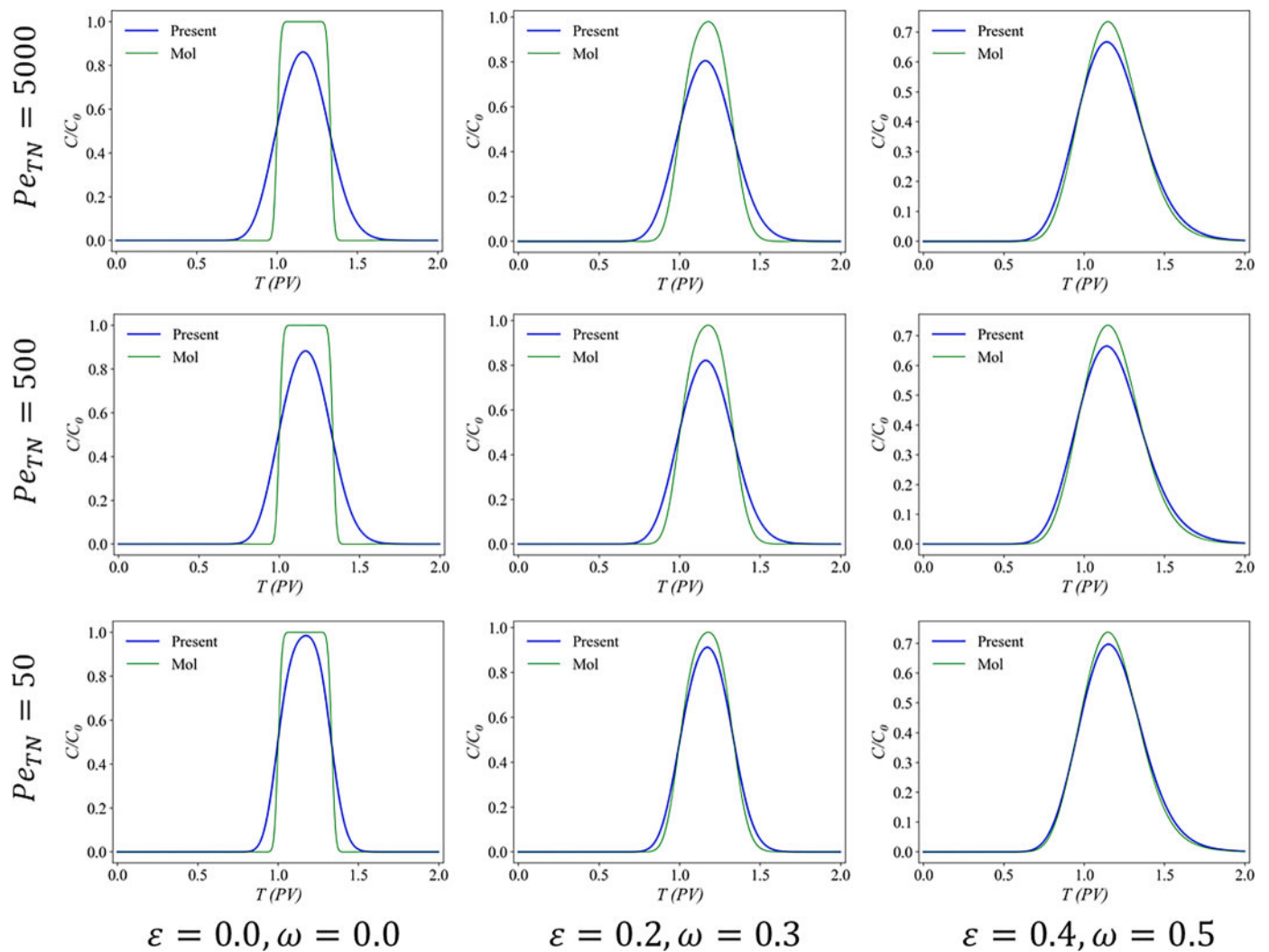


Fig. 19. Comparison of breakthrough curves for different Pe_{TN} and combined tube radius disorder ε and tube length disorder ω . ‘Present’ and ‘Mol’ denote the results predicted by the present model and the model ignores pore-scale shear dispersion, respectively.

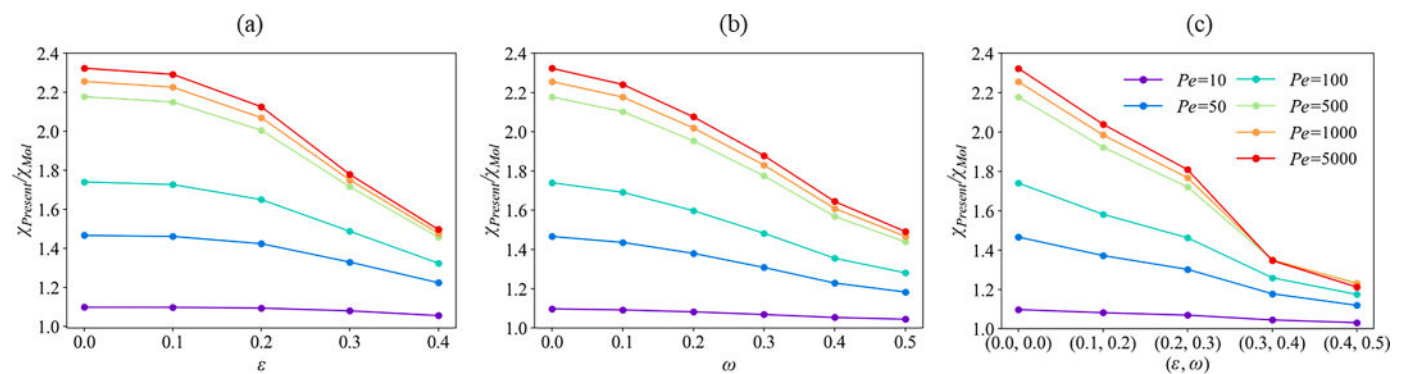


Fig. 20. The impact of pore-scale shear dispersion on solute transport, characterized by $\chi_{present}/\chi_{Mol}$ for different (a) tube radius disorders ε , (b) tube length disorders ω , and (c) combined tube radius disorders ε and tube length disorders ω . $\chi_{present}$ and χ_{Mol} represent the temporal width of breakthrough curves predicted by the present model and the model that ignores pore-scale shear dispersion, respectively.

CRedit authorship contribution statement

Yang Liu: Investigation, Validation, Writing – original draft, Software. **Wenbo Gong:** Validation, Writing – original draft. **Han Xiao:** Investigation, Writing – original draft. **Moran Wang:** Conceptualization, Formal analysis, Methodology, Supervision, Project

administration, Writing – review & editing.

Declaration of Competing Interest

The authors declare that they have no known competing financial interests or personal relationships that could have appeared to influence

the work reported in this paper.

Data availability

No data was used for the research described in the article.

Acknowledgments

This work is financially supported by the National Key Research and Development Program of China (No. 2019YFA0708704) and the NSF grant of China (No. 12272207, U1837602).

Appendix A. Random walk: algorithm and verification

To simplify the simulation procedure, the random walk algorithm is based on the following assumptions: (1) a fully developed Poiseuille flow exists in the pipe, allowing for the analytical determination of the velocity profile; (2) the size of solute particles is negligible compared to the pore size; (3) the solution is sufficiently dilute that mass transfer has no feedback on fluid flow; and (4) the interaction between particles and the inertia of solute particles are negligible.

The random walk algorithm follows the following steps:

- (1) In step 1, the velocity profile in the tube is analytically determined according to the cross-sectional shape;
- (2) In step 2, a population of particles is released at the origin plane ($x = 0$);
- (3) In step 3, particles are moved alternately by advection and diffusion, and their trajectories are recorded;

Step 3 is depicted in Fig. A.1 with a circular pipe. After a time step Δt , the advective length of particles along the streamlines is given by

$$\Delta x_{adv} = U_{(y,z)} \Delta t. \quad (A1)$$

In the diffusive step, particles undergo movement in a random direction as defined by $(R_{dif}, \theta, \varphi)$ in a spherical coordinate system, where $\cos\theta$ and φ are uniformly distributed in the range of $[-1, 1]$ and $[0, 2\pi]$, respectively. The diffusive length R_{dif} is

$$R_{dif} = \sqrt{6D_m \Delta t}, \quad (A2)$$

where D_m is the molecular diffusion coefficient. The diffusive displacement is then transformed into a Cartesian coordinate system as

$$\Delta x_{dif} = R_{dif} \sin\theta \sin\varphi, \quad (A3)$$

$$\Delta y_{dif} = R_{dif} \sin\theta \cos\varphi, \quad (A4)$$

$$\Delta z_{dif} = R_{dif} \cos\theta. \quad (A5)$$

Throughout the time step Δt , the total displacement $\Delta \mathbf{r}$ is

$$\Delta \mathbf{r} = (\Delta x_{adv} + \Delta x_{dif}, \Delta y_{dif}, \Delta z_{dif}). \quad (A6)$$

The bounce-back boundary condition is adopted at solid walls for diffusion.

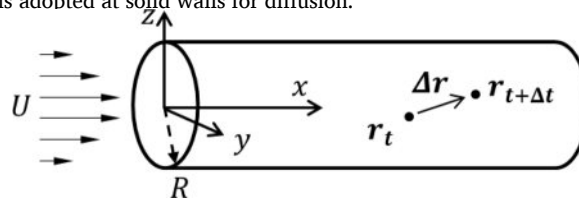


Fig. A.1. Schematic of dispersion in a circular pipe. \mathbf{r}_t and $\mathbf{r}_{t+\Delta t}$ are coordinates of a particle at the current step and the next moment, respectively, and $\Delta \mathbf{r}$ is the displacement.

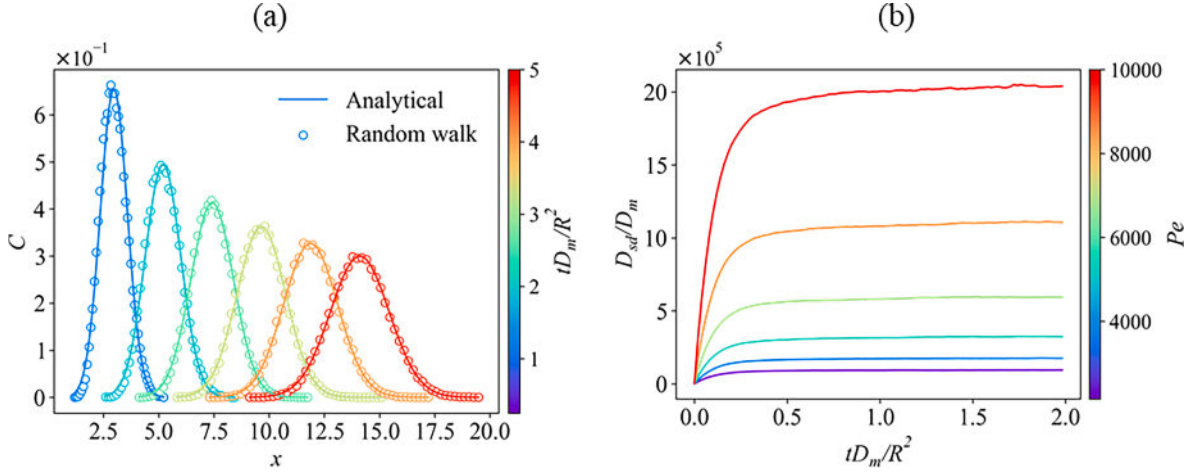


Fig. A.2. (a) The comparison of concentration profiles for Taylor dispersion in a circular tube at $Pe = 300$. Lines and circles are rendered by the dimensionless flow time tD_m/R^2 . (b) The evolution of the dimensionless shear dispersion coefficient D_{sd}/D_m versus dimensionless flow time tD_m/R^2 .

The setups of random walk simulations are described as follows. The inscribed radius R of pipes is fixed at 0.01m , and the molecular diffusion coefficient D_m is $10^{-9}\text{m}^2/\text{s}$. To ensure reliable and statistically converged results, a slug containing 10^5 particles is tracked in the random walk simulations. All the random walk simulations are performed on a personal computer, with each simulation taking approximately 50 s to complete. The accuracy and performance of the algorithm are verified using Taylor dispersion at $Pe = 300$, where the cross-sectional averaged concentration C is analytically given by

$$C(x, t) = \frac{n_0}{\sqrt{4\pi D_{sd}t}} \exp\left(-\frac{(x - U_{ave}t)^2}{4D_{sd}t}\right), \quad (\text{A7})$$

where n_0 is the number of particles and U_{ave} is the average velocity. D_{sd} is the Taylor dispersion coefficient calculated from Eq. (16). The reliability of the algorithm is confirmed by the excellent agreement between the predicted concentration profiles at different moments and the corresponding analytical solutions, as shown in Fig. A2(a).

Appendix B. Derivation of Eq. (17)

According to the work of Taghizadeh et al. (2020), the pre-asymptotic shear dispersion coefficient of circular pipes can be expressed as:

$$\frac{D_{sd}/D_m - 1}{\kappa Pe^2} = 1 - \frac{4}{\kappa} \sum_{n=1}^{\infty} \left[\frac{J_3(\lambda_n)}{\lambda_n^2 J_0(\lambda_n)} \right]^2 \exp\left(-\lambda_n^2 \frac{D_m}{R^2} t\right), \quad (\text{B1})$$

where J_0 , J_1 , and J_3 are Bessel functions, and the λ_n is the n^{th} eigenvalue which satisfies

$$J_1(\lambda_n) = 0 \quad (\lambda_1 < \lambda_2 < \dots < \lambda_n). \quad (\text{B2})$$

The coefficients of the exponential terms in Eq. (B1) satisfy the equation:

$$\frac{4}{\kappa} \sum_{n=1}^{\infty} \left[\frac{J_3(\lambda_n)}{\lambda_n^2 J_0(\lambda_n)} \right]^2 = 1. \quad (\text{B3})$$

The infinite series in Eq. (B1) can be rearranged as

$$\begin{aligned} \frac{4}{\kappa} \sum_{n=1}^{\infty} \left[\frac{J_3(\lambda_n)}{\lambda_n^2 J_0(\lambda_n)} \right]^2 \exp\left(-\lambda_n^2 \frac{D_m}{R^2} t\right) &= \frac{4}{\kappa} \left[\frac{J_3(\lambda_1)}{\lambda_1^2 J_0(\lambda_1)} \right]^2 \exp\left(-\lambda_1^2 \frac{D_m}{R^2} t\right) \\ &+ \frac{4}{\kappa} \sum_{n=2}^{\infty} \left[\frac{J_3(\lambda_n)}{\lambda_n^2 J_0(\lambda_n)} \right]^2 \exp\left(-\lambda_n^2 \frac{D_m}{R^2} t\right). \end{aligned} \quad (\text{B4})$$

Since $\lambda_1 < \lambda_2 < \dots < \lambda_n$, we can deduce that:

$$\begin{aligned} \frac{4}{\kappa} \sum_{n=1}^{\infty} \left[\frac{J_3(\lambda_n)}{\lambda_n^2 J_0(\lambda_n)} \right]^2 \exp\left(-\lambda_n^2 \frac{D_m}{R^2} t\right) &\leq \frac{4}{\kappa} \left[\frac{J_3(\lambda_1)}{\lambda_1^2 J_0(\lambda_1)} \right]^2 \exp\left(-\lambda_1^2 \frac{D_m}{R^2} t\right) \\ &+ \frac{4}{\kappa} \sum_{n=2}^{\infty} \left[\frac{J_3(\lambda_n)}{\lambda_n^2 J_0(\lambda_n)} \right]^2 \exp\left(-\lambda_1^2 \frac{D_m}{R^2} t\right). \end{aligned} \quad (\text{B5})$$

Using Eq. (B5), the ratio of the first term to the entire infinite series can be expressed as

$$\frac{\frac{4}{\kappa} \left[\frac{J_3(\lambda_1)}{\lambda_1^2 J_0(\lambda_1)} \right]^2 \exp\left(-\lambda_1^2 \frac{D_m}{R^2} t\right)}{\frac{4}{\kappa} \sum_{n=1}^{\infty} \left[\frac{J_3(\lambda_n)}{\lambda_n^2 J_0(\lambda_n)} \right]^2 \exp\left(-\lambda_n^2 \frac{D_m}{R^2} t\right)} \geq \frac{\frac{4}{\kappa} \left[\frac{J_3(\lambda_1)}{\lambda_1^2 J_0(\lambda_1)} \right]^2}{\frac{4}{\kappa} \left[\frac{J_3(\lambda_1)}{\lambda_1^2 J_0(\lambda_1)} \right]^2 + \frac{4}{\kappa} \sum_{n=2}^{\infty} \left[\frac{J_3(\lambda_n)}{\lambda_n^2 J_0(\lambda_n)} \right]^2}. \tag{B6}$$

By substituting Eq. (B3) and $\lambda_1 = 3.83$ into Eq. (B6), the following result is obtained:

$$\frac{\frac{4}{\kappa} \left[\frac{J_3(\lambda_1)}{\lambda_1^2 J_0(\lambda_1)} \right]^2 \exp\left(-\lambda_1^2 \frac{D_m}{R^2} t\right)}{\frac{4}{\kappa} \sum_{n=1}^{\infty} \left[\frac{J_3(\lambda_n)}{\lambda_n^2 J_0(\lambda_n)} \right]^2 \exp\left(-\lambda_n^2 \frac{D_m}{R^2} t\right)} \geq 0.9707, \tag{B7}$$

which indicates that the relative error of approximating the entire infinite series with just the first term is less than 3%. By truncating the infinite series to its first order, Eq. (B1) can be simplified as

$$\frac{D_{sd}/D_m - 1}{\kappa P e^2} = 1 - \alpha \cdot \exp\left(-\beta \frac{D_m}{R^2} t\right), \tag{B8}$$

where $\alpha = \frac{4}{\kappa} \left[\frac{J_3(\lambda_1)}{\lambda_1^2 J_0(\lambda_1)} \right]^2$ and $\beta = \lambda_1^2$.

Naturally, Eq. (B8) can be extended to pipes with square and equilateral triangular cross-sections, where α and β are coefficients dependent on the shape of pipe cross-sections.

Appendix C. Setups of OpenFOAM simulations

We employ the open-source software, OpenFOAM, for performing DNS simulations of solute transport in Section 3.1.

The flow field is solved using the simpleFoam application, where the laminar model and the steady state time scheme are employed. The convergence criteria for terminating the flow simulation are set as 10^{-5} for pressure p and 10^{-7} for velocity U . The boundary conditions are defined as follows:

$$\frac{\partial U}{\partial n} \Big|_{\partial \Omega_{in/out}} = 0, \quad U|_{\Gamma_w} = 0, \quad p|_{\partial \Omega_{in/out}} = p_{in/out}, \quad \frac{\partial p}{\partial n} \Big|_{\Gamma_w} = 0, \tag{C1}$$

where $\partial \Omega_{in/out}$ denotes the inlet/outlet boundaries and Γ_w is the solid-fluid interface.

We simulate solute transport at different Pe_{TN} by varying the molecular diffusion coefficient D_m . The concentration field is solved using the scalarTransportFoam application, where the divergence term is discretized with the Gauss vanLeer scheme. The time step is chosen as 0.05s to ensure that the average Courant number remains below 0.1. At the inlet, a solute pulse with a concentration of C_0 is applied. The boundary conditions are defined as follows:

$$C|_{\partial \Omega_{in}} = C_0 (1 - f(t - t_p)), \quad \frac{\partial C}{\partial n} \Big|_{\partial \Omega_{out}} = 0, \quad \frac{\partial C}{\partial n} \Big|_{\Gamma_w} = 0, \tag{C2}$$

where $f(t)$ is the Heaviside function and t_p is the pulse duration.

Appendix D. Geometrical disorder of the bead pack and sand pack

The pore size distribution and conduit length distribution of the reconstructed bead pack (Section 3.2) and sand pack (Section 3.3) are displayed in the following figure.

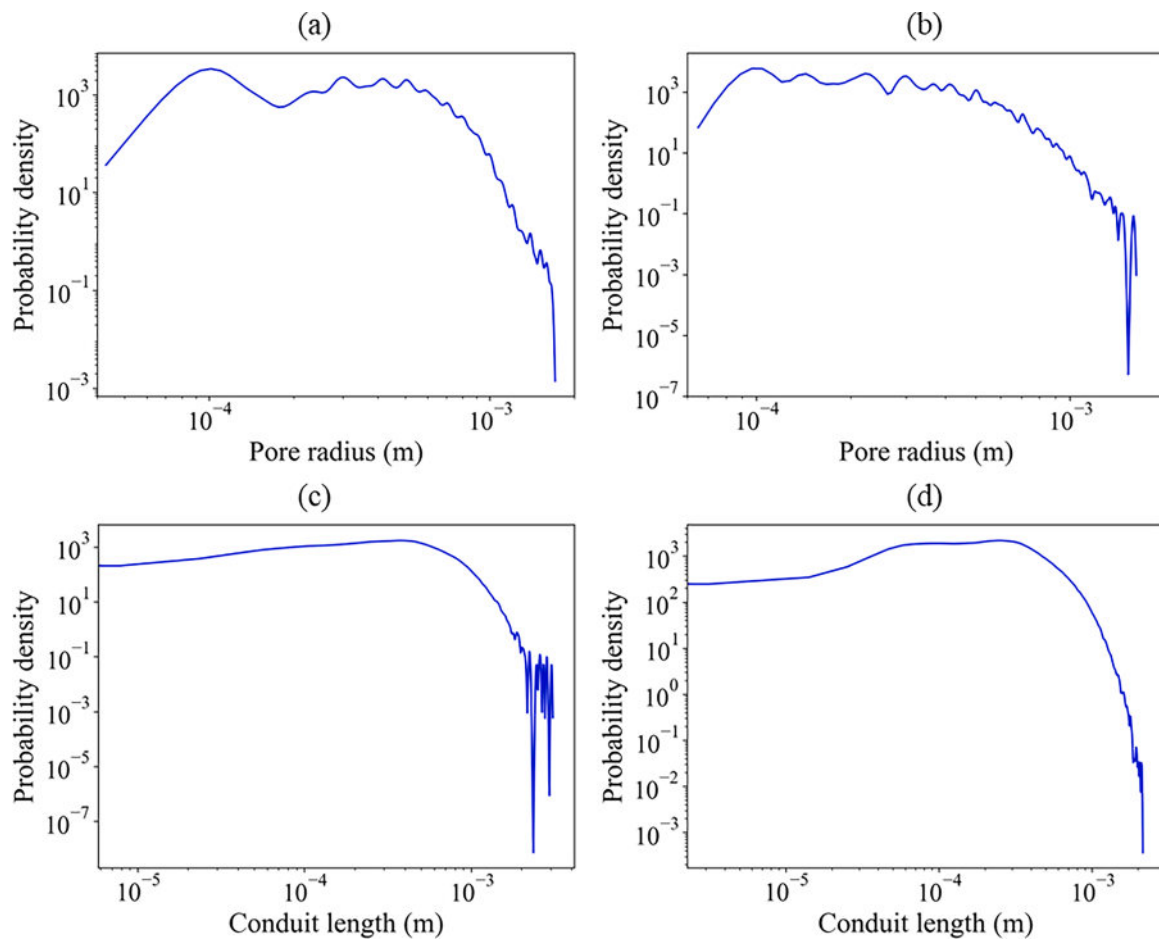


Fig. D.1. Pore size distribution (top row) and conduit length distribution (bottom row) of the bead pack (a, c) in Section 3.2, and the sand pack (b, d) in Section 3.3.

References

- Acharya, R.C., Van der Zee, S.E.A.T.M., Leijnse, A., 2007. Approaches for modeling longitudinal dispersion in pore-networks. *Adv. Water Resour.* 30 (2), 261–272.
- Ananthakrishnan, V., Gill, W.N., Barduhn, A.J., 1965. Laminar dispersion in capillaries: part I. *Mathematical analysis.* *AIChE J.* 11 (6), 1063–1072.
- Aris, R., 1956. On the dispersion of a solute in a fluid flowing through a tube. *Proc. R. Soc. Lond. A* 235 (1200), 67–77.
- Babaei, M., Joekar-Niasar, V., 2016. A transport phase diagram for pore-level correlated porous media. *Adv. Water Resour.* 92, 23–29.
- Bear, J., 2013. *Dynamics of Fluids in Porous Media.* Courier Corporation.
- Berg, M., Davit, Y., Quintard, M., Lorthois, S., 2020. Modelling solute transport in the brain microcirculation: is it really well mixed inside the blood vessels? *J. Fluid Mech.* 884, A39.
- Bernabé, Y., Wang, Y., Qi, T., Li, M., 2016. Passive advection-dispersion in networks of pipes: effect of connectivity and relationship to permeability. *J. Geophys. Res.: Solid Earth* 121 (2), 713–728.
- Bhattad, P., Willson, C.S., Thompson, K.E., 2011. Effect of network structure on characterization and flow modeling using X-ray micro-tomography images of granular and fibrous porous media. *Transp. Porous Media* 90 (2), 363–391.
- Bijeljic, B., Muggeridge, A.H., Blunt, M.J., 2004. Pore-scale modeling of longitudinal dispersion. *Water Resour. Res.* 40 (11), W11501.
- Blunt, M.J., Bijeljic, B., Dong, H., Gharbi, O., Iglauer, S., Mostaghimi, P., Paluszny, A., Pentland, C., 2013. Pore-scale imaging and modelling. *Adv. Water Resour.* 51, 197–216.
- Bondino, I., Hamon, G., Kallel, W., Kac, D., 2013. Relative Permeabilities from simulation in 3D rock models and equivalent pore networks: critical review and way forward. *Petrophys.-SPWLA J. Format. Eval. Reserv. Descript.* 54 (06), 538–546.
- Bultreys, T., Lin, Q., Gao, Y., Raeini, A.Q., AlRatout, A., Bijeljic, B., Blunt, M.J., 2018. Validation of model predictions of pore-scale fluid distributions during two-phase flow. *Phys. Rev. E* 97 (5), 053104.
- Chen, S., Doolen, G.D., 1998. Lattice Boltzmann method for fluid flows. *Annu. Rev. Fluid Mech.* 30 (1), 329–364.
- Chen, S., Qin, C., Guo, B., 2020. Fully implicit dynamic pore-network modeling of two-phase flow and phase change in porous media. *Water Resour. Res.* 56 (11) e2020WR028510.
- Chen, S., Jiang, J., Guo, B., 2021. A pore-network-based upscaling framework for the nanoconfined phase behavior in shale rocks. *Chem. Eng. J.* 417, 129210.
- Cheng, T., Yang, H., Sun, S., 2022. Parallel fully coupled methods for bound-preserving solution of subsurface flow and transport in porous media. *J. Comput. Phys.* 470, 111537.
- Dentz, M., Felipe, de Barros, P.J., 2015. Mixing-scale dependent dispersion for transport in heterogeneous flows. *J. Fluid Mech.* 777, 178–195.
- Dentz, M., Le Borgne, T., Englert, A., Bijeljic, B., 2011. Mixing, spreading and reaction in heterogeneous media: a brief review. *J. Contam. Hydrol.* 120, 1–17.
- Dentz, M., Icardi, M., Hidalgo, J.J., 2018. Mechanisms of dispersion in a porous medium. *J. Fluid Mech.* 841, 851–882.
- Dong, H., Blunt, M.J., 2009. Pore-network extraction from micro-computerized-tomography images. *Phys. Rev. E* 80 (3), 036307.
- Esteves, B.F., Lage, P.L.C., Couto, P., Kovscek, A.R., 2020. Pore-network modeling of single-phase reactive transport and dissolution pattern evaluation. *Adv. Water Resour.* 145, 103741.
- Ferrari, A., Lunati, I., 2014. Inertial effects during irreversible meniscus reconfiguration in angular pores. *Adv. Water Resour.* 74, 1–13.
- Golparvar, A., Zhou, Y., Wu, K., Ma, J., Yu, Z., 2018. A comprehensive review of pore scale modeling methodologies for multiphase flow in porous media. *Adv. Geo-Energy Res.* 2 (4), 418–440.
- Gostick, J.T., 2017. Versatile and efficient pore network extraction method using marker-based watershed segmentation. *Phys. Rev. E* 96 (2), 023307.
- Gramling, C.M., Harvey, C.F., Meigs, L.C., 2002. Reactive transport in porous media: a comparison of model prediction with laboratory visualization. *Environ. Sci. Technol.* 36 (11), 2508–2514.
- Guo, B., Mehmani, Y., Tchelepi, H.A., 2019. Multiscale formulation of pore-scale compressible Darcy-Stokes flow. *J. Comput. Phys.* 397.
- He, M., Zhou, Y., Wu, K., Hu, Y., Feng, D., Zhang, T., Liu, Q., Li, X., 2021. Pore network modeling of thin water film and its influence on relative permeability curves in tight formations. *Fuel* 289, 119828.

- Hidalgo, J.J., Dentz, M., 2018. Mixing across fluid interfaces compressed by convective flow in porous media. *J. Fluid Mech.* 838, 105–128.
- Khayrat, K., Jenny, P., 2017. A multi-scale network method for two-phase flow in porous media. *J. Comput. Phys.* 342, 194–210.
- Khayrat, K., Epp, R., Jenny, P., 2018. Approximate multiscale flow solver for unstructured pore networks. *J. Comput. Phys.* 372, 62–79.
- Kim, D., Peters, C.A., Lindquist, W.B., 2011. Upscaling geochemical reaction rates accompanying acidic CO₂-saturated brine flow in sandstone aquifers. *Water Resour. Res.* 47 (1), W01505.
- Koch, D.L., Brady, J.F., 1985. Dispersion in fixed beds. *J. Fluid Mech.* 154, 399–427.
- Koplik, J., Redner, S., Wilkinson, D., 1988. Transport and dispersion in random networks with percolation disorder. *Phys. Rev. A* 37 (7), 2619.
- Kou, J., Wang, X., Chen, H., Sun, S., 2023. An efficient bound-preserving and energy stable algorithm for compressible gas flow in porous media. *J. Comput. Phys.* 473, 111751.
- Li, K., Mehmani, Y., 2023. A pore-level multiscale method for the elastic deformation of fractured porous media. *J. Comput. Phys.* 483.
- Li, L., Peters, C.A., Celia, M.A., 2006. Upscaling geochemical reaction rates using pore-scale network modeling. *Adv. Water Resour.* 29 (9), 1351–1370.
- Li, S., Raouf, A., Schotting, R., 2014. Solute dispersion under electric and pressure driven flows; pore scale processes. *J. Hydrol.* 517, 1107–1113.
- Liu, Y., Gong, W., Zhao, Y., Jin, X., Wang, M., 2022a. A pore-throat segmentation method based on local hydraulic resistance equivalence for pore-network modeling. *Water Resour. Res.* 58 (12) e2022WR033142.
- Liu, J., Tang, Q., Kou, J., Xu, D., Zhang, T., Sun, S., 2022b. A quantitative study on the approximation error and speed-up of the multi-scale MCMC (Monte Carlo Markov chain) method for molecular dynamics. *J. Comput. Phys.* 469, 111491.
- Mason, G., Morrow, N.R., 1991. Capillary behavior of a perfectly wetting liquid in irregular triangular tubes. *J. Colloid Interface Sci.* 141 (1), 262–274.
- Mauri, R., Haber, S., 1991. Time-dependent dispersion of small particles in rectangular conduits. *SIAM J. Appl. Math.* 51 (6), 1538–1555.
- Mehmani, Y., Balhoff, M.T., 2015. Eulerian network modeling of longitudinal dispersion. *Water Resour. Res.* 51 (10), 8586–8606.
- Mehmani, Y., Li, K., 2023. A multiscale preconditioner for microscale deformation of fractured porous media. *J. Comput. Phys.* 482.
- Mehmani, Y., Tchelepi, H.A., 2018. Multiscale computation of pore-scale fluid dynamics: single-phase flow. *J. Comput. Phys.* 375, 1469–1487.
- Mehmani, Y., Tchelepi, H.A., 2019. Multiscale formulation of two-phase flow at the pore scale. *J. Comput. Phys.* 389, 164–188.
- Mehmani, Y., Xu, K., 2022. Pore-network modeling of Ostwald ripening in porous media: how do trapped bubbles equilibrate? *J. Comput. Phys.* 457, 111041.
- Mehmani, Y., Castelletto, N., Tchelepi, H.A., 2021. Multiscale formulation of frictional contact mechanics at the pore scale. *J. Comput. Phys.* 430.
- Øren, P.E., Bakke, S., 2003. Reconstruction of Berea sandstone and pore-scale modelling of wettability effects. *J. Pet. Sci. Eng.* 39 (3–4), 177–199.
- Patzek, T., Silin, D.B., 2001. Shape factor and hydraulic conductance in noncircular capillaries: I. One-phase creeping flow. *J. Colloid Interface Sci.* 236 (2), 295–304.
- Puyguraud, A., Gouze, P., Dentz, M., 2019. Upscaling of anomalous pore-scale dispersion. *Transp. Porous Media* 128 (2), 837–855.
- Raje, D.S., Kapoor, V., 2000. Experimental study of bimolecular reaction kinetics in porous media. *Environ. Sci. Technol.* 34 (7), 1234–1239.
- Raman, S.L.B., Jha, K., Lake, L.W., 2011. Effect of diffusion on dispersion. *SPE J.* 16 (1), 65–77.
- Roslin, A., Pokrajac, D., Zhou, Y., 2019. Cleat structure analysis and permeability simulation of coal samples based on micro-computed tomography (micro-CT) and scan electron microscopy (SEM) technology. *Fuel* 254, 115579.
- Sadeghi, M.A., Aghighi, M., Barralet, J., Gostick, J.T., 2017. Pore network modeling of reaction-diffusion in hierarchical porous particles: the effects of microstructure. *Chem. Eng. J.* 330, 1002–1011.
- Sadeghi, M.A., Agnaou, M., Barralet, J., Gostick, J., 2020. Dispersion modeling in pore networks: a comparison of common pore-scale models and alternative approaches. *J. Contam. Hydrol.* 228, 103578.
- Saffman, P.G., 1959. A theory of dispersion in a porous medium. *J. Fluid Mech.* 6 (03), 321–349.
- Sahimi, M., Jue, V.L., 1989. Diffusion of large molecules in porous media. *Phys. Rev. Lett.* 62 (6), 629.
- Sahimi, M., Heiba, A.A., Davis, H.T., Scriven, L., 1986. Dispersion in flow through porous media—II. Two-phase flow. *Chem. Eng. Sci.* 41 (8), 2123–2136.
- Sholokhova, Y., Kim, D., Lindquist, W.B., 2009. Network flow modeling via lattice-Boltzmann based channel conductance. *Adv. Water Resour.* 32 (2), 205–212.
- Taghizadeh, E., Valdés-Parada, F.J., Wood, B.D., 2020. Preasymptotic Taylor dispersion: evolution from the initial condition. *J. Fluid Mech.* 889, A5.
- Tartakovsky, A.M., Meakin, P., Scheibe, T.D., Wood, B.D., 2007. A smoothed particle hydrodynamics model for reactive transport and mineral precipitation in porous and fractured porous media. *Water Resour. Res.* 43 (5), W05437.
- Taylor, G.I., 1953. Dispersion of soluble matter in solvent flowing slowly through a tube. *Proc. R. Soc. Lond. A* 219 (1137), 186–203.
- van Gorp, R., van der Heijden, M., Sadeghi, M.A., Gostick, J., Forner-Cuenca, A., 2023. Bottom-up design of porous electrodes by combining a genetic algorithm and a pore network model. *Chem. Eng. J.* 455, 139947.
- Wang, C., Wu, K., Scott, G.G., Akisanya, A.R., Gan, Q., Zhou, Y., 2020. A new method for pore structure quantification and pore network extraction from SEM images. *Energy Fuels* 34 (1), 82–94.
- Weishaupt, K., Joekar-Niasar, V., Helmig, R., 2019. An efficient coupling of free flow and porous media flow using the pore-network modeling approach. *J. Comput. Phys.: X* 1.
- Xie, C., Lei, W., Balhoff, M.T., Wang, M., Chen, S., 2021. Self-adaptive preferential flow control using displacing fluid with dispersed polymers in heterogeneous porous media. *J. Fluid Mech.* 906, A10.
- Yan, Z., Yang, X., Li, S., Hilpert, M., 2017. Two-relaxation-time lattice Boltzmann method and its application to advective-diffusive-reactive transport. *Adv. Water Resour.* 109, 333–342.
- Yang, X., Scheibe, T.D., Richmond, M.C., Perkins, W.A., Vogt, S.J., Codd, S.L., Seymour, J.D., McKinley, M.I., 2013. Direct numerical simulation of pore-scale flow in a bead pack: comparison with magnetic resonance imaging observations. *Adv. Water Resour.* 54, 228–241.
- Yang, X., Mehmani, Y., Perkins, W.A., Pasquali, A., Schönherr, M., Kim, K., Perego, M., Parks, M.L., Trask, N., Balhoff, M.T., Richmond, M.C., Geier, M., Krafczyk, M., Luo, L.-S., Tartakovsky, A.M., Scheibe, T.D., 2016. Intercomparison of 3D pore-scale flow and solute transport simulation methods. *Adv. Water Resour.* 95, 176–189.
- Yi, Z., Lin, M., Jiang, W., Zhang, Z., Li, H., Gao, J., 2017. Pore network extraction from pore space images of various porous media systems. *Water Resour. Res.* 53 (4), 3424–3445.
- Zhang, T., Salama, A., Sun, S., El-Amin, M.F., 2015. Pore network modeling of drainage process in patterned porous media: a quasi-static study. *J. Comput. Sci.* 9, 64–69.
- Zheng, J., Ju, Y., Wang, M., 2018. Pore-scale modeling of spontaneous imbibition behavior in a complex shale porous structure by pseudopotential lattice Boltzmann method. *J. Geophys. Res.: Solid Earth* 123 (11), 9586–9600.